Implications of laterally varying scattering properties for subsurface monitoring with coda wave sensitivity kernels: application to volcanic and fault zone setting

Chantal Dinther, Ludovic Margerin, Michel Campillo

JGR Solid Earth

RESEARCH ARTICLE
10.1029/2021JB022554

Implications of Laterally Varying Scattering Properties for Subsurface Monitoring With Coda Wave Sensitivity Kernels: Application to Volcanic and Fault Zone Setting

Chantal van Dinther[1], Ludovic Margerin[2], and Michel Campillo[1]

[1]Université Grenoble Alpes, CNRS, ISTerre, Grenoble, France, [2]Institut de Recherche en Astrophysique et Planétologie, Université Toulouse III Paul Sabatier, CNRS, CNES, Toulouse, France

Key Points:

- A non-uniform distribution of scattering strength can have a profound impact on the spatio-temporal sensitivity of coda waves
- We illustrate this using Monte Carlo simulations for models with either a volcanic, fault zone, or two half-spaces setting
- The mean intensity, specific intensity, and energy flux, is key to understanding the decorrelation, travel-time, and scattering kernels, respectively

Supporting Information:

Supporting Information may be found in the online version of this article.

Correspondence to:

C. van Dinther,
chantal.van-dinther@univ-grenoble-alpes.fr

Citation:

van Dinther, C., Margerin, L., & Campillo, M. (2021). Implications of laterally varying scattering properties for subsurface monitoring with coda wave sensitivity kernels: Application to volcanic and fault zone setting. *Journal of Geophysical Research: Solid Earth*, *126*, e2021JB022554. https://doi.org/10.1029/2021JB022554

Received 8 JUN 2021
Accepted 29 NOV 2021

Abstract Monitoring changes of seismic properties at depth can provide a first-order insight into Earth's dynamic evolution. Coda wave interferometry is the primary tool for this purpose. This technique exploits small changes of waveforms in the seismic coda and relates them to temporal variations of attenuation or velocity at depth. While most existing studies assume statistically homogeneous scattering strength in the lithosphere, geological observations suggest that this hypothesis may not be fulfilled in active tectonic or volcanic areas. In a numerical study we explore the impact of a non-uniform distribution of scattering strength on the spatio-temporal sensitivity of coda waves. Based on Monte Carlo simulation of the radiative transfer process, we calculate sensitivity kernels for three different observables, namely travel-time, decorrelation, and intensity. Our results demonstrate that laterally varying scattering properties can have a profound impact on the sensitivities of coda waves. Furthermore, we demonstrate that the knowledge of the mean intensity, specific intensity, and energy flux, governed by spatial variation of scattering strength, is key to understanding the decorrelation, travel-time, and scattering kernels, respectively. A number of previous works on coda wave sensitivity kernels neglect the directivity of energy fluxes by employing formulas extrapolated from the diffusion approximation. In this work, we demonstrate and visually illustrate the importance of the use of specific intensity for the travel-time and scattering kernels, in the context of volcanic and fault zone setting models. Our results let us foresee new applications of coda wave monitoring in environments of high scattering contrast.

Plain Language Summary To monitor the evolution of the dynamic Earth, seismologists use a part of the seismic record called "coda," which is composed of waves that have bounced multiple times off heterogeneities of the crust. The coda is extremely sensitive to weak perturbations of propagation properties induced by Earth's tectonic and volcanic activity. The correct physical modeling of coda waves is therefore key to unravel the rich information encoded in their waveforms. A limitation of current seismological monitoring techniques is the neglect of strong lateral variations of coda waves propagation properties documented by geological observations. Our work focuses specifically on this aspect. We provide a complete theoretical and numerical framework to model and understand the spatial and temporal sensitivity of coda waves to medium perturbations in complex geological settings. Using simple but realistic models of a fault zone and a volcano, we illustrate the profound impact of non-uniform scattering properties on the coda wave sensitivity, which in turn determines the ability of seismologists to correctly retrieve the magnitude and location of physical changes in the crust. Our results let us foresee new applications of coda wave monitoring in environments of high scattering contrast, such as volcanic and fault zone settings.

1. Introduction

With the recent advancements in seismic sensor techniques and the rapid deployment of (dense) seismic arrays over the last decade, there has been a surge in the number of monitoring studies aiming to capture the dynamic evolution of the subsurface. Due to scattering, coda waves sample a large volume of the subsurface densely for long propagation times and are thus sensitive to weak changes of the medium. Consequently, coda waves may be more suitable to characterize temporal variations of the Earth's crust than direct waves, which only sample a narrow volume along the ray path between the (virtual) source and detector. Poupinet et al. (1984) were first to demonstrate the feasibility of monitoring weak changes in apparent velocity caused by fault activity in California using coda waves. Poupinet et al. (1984) derived these global medium changes by measuring the phase shift between the coda of earthquake doublets. In numerical and lab experiments, the extreme sensitivity of the

seismic coda to temporal medium changes has also been demonstrated by Snieder et al. (2002). Later, detection of temporal medium changes has been successfully applied using the coda of earthquake records or the coda of ambient noise cross-correlations in numerous settings including but not limited to: volcanoes (e.g., Brenguier et al., 2016; Hirose et al., 2017; Mao et al., 2019; Mordret et al., 2010; Obermann, Planès, Larose, Sens-Schönfelder, & Campillo, 2013; Sánchez-Pastor et al., 2018; Sens-Schönfelder & Wegler, 2006), fault zones (e.g., Brenguier et al., 2008; Chen et al., 2010; Peng & Ben-Zion, 2006; Rivet et al., 2014; Roux & Ben-Zion, 2014; Schaff & Beroza, 2004; Wu et al., 2009), and CO_2 and geothermal reservoirs (Hillers et al., 2015, 2020; Obermann et al., 2015).

Although measurements of temporal medium changes are interesting in their own right, knowledge about their spatial location is necessary to gain more insight into the processes that occur at depth. Regionalization of data can yield a first-order estimate on the spatial distribution, but a preferable approach is to perform a (linear) inversion using so-called sensitivity kernels. In loose terms, these spatial weighting functions provide information on the parts of the medium that have preferentially been sampled by the waves in a probabilistic sense. The first travel-time sensitivity kernels for coda wave interferometry have been introduced by Pacheco and Snieder (2005) under the diffusion approximation. Shortly after, Pacheco and Snieder (2006) provided probabilistic kernels for the single scattering regime. Obermann, Planès, Larose, and Campillo (2013) applied these kernels to invert for structural and temporal velocity changes around the Piton de la Fournaise volcano on Reunion Island. To detect and locate medium changes caused by the M_w 7.9, 2008 earthquake in Wenchuan in China, Obermann et al. (2019) used a 3D kernel combining the sensitivity of body and surface waves. Although the results of the authors were very promising, Margerin et al. (2016) raised questions about the formulas used to compute the sensitivity kernels, since the works rely on an extrapolation of a formula established in the diffusion regime. Margerin et al. (2016) demonstrated that knowledge of the angular distribution of the energy fluxes of coda waves is required for an accurate prediction of sensitivities, valid for an arbitrary distribution of heterogeneities and all propagation regimes. The authors obtained this result by using a radiative transfer approach, which directly predicts specific intensities. Snieder et al. (2019) derive different travel-time sensitivity kernels for acoustic and elastic waves, where the one for the 2D acoustic case based on radiative transfer theory follows a similar derivation as Margerin et al. (2016). Additionally, the authors derived separate travel-time sensitivity kernels for diffusive acoustic waves and diffusive elastic waves. Building on the work of Snieder et al. (2019) and Duran et al. (2020) developed a numerical approach to derive elastic and acoustic decorrelation sensitivity kernels for statistically uniform media. Other developments on sensitivity kernels focus on the sensitivity as a function of depth. Obermann et al. (2016) and Obermann, Planès, Larose, and Campillo (2013) showed that a linear combination of the 2D surface wave and 3D body wave kernels are a decent proxy to describe the sensitivity as function of lapse-time and depth. A formal approach to couple body and surface waves is provided by Margerin et al. (2019), leading to a specific formulation of kernels (Barajas, 2021).

Most of these studies on sensitivity kernels provide a solution for statistically homogeneous scattering media, although the interest in extending the sensitivity kernels to non-uniform media is growing, which is especially interesting for monitoring volcanic and fault zone settings. Wegler and Lühr (2001) derived attenuation parameters around the Merapi volcano in Indonesia. The authors found a scattering mean free path (ℓ) as low as 100 m for S waves in the frequency band of 4–20 Hz. They also reported that the scattering attenuation is at least one order of magnitude larger than the intrinsic attenuation around Merapi. Later, Yoshimoto et al. (2006) estimated scattering attenuation in the north-eastern part of Honshu in Japan. For this volcanic area the authors analyzed the coda of earthquake records and reported a scattering coefficient of 0.01 km^{-1} for the frequency of 10 Hz. Another study that analyzed the coda of seismograms in a volcanic setting in Japan found the scattering mean free path for *P* and *S* waves to be as short as 1 km for the 8–16 Hz frequency band (Yamamoto & Sato, 2010). Recently, Hirose et al. (2019) derived a scattering mean free path ~2 km at Sakurajima volcano in Japan, which is much smaller than in the surrounding rock. In a recent study on the western part of the North Anatolian Fault Zone (NAFZ) van Dinther et al. (2021) also found a strong contrast in scattering (approximately factor of 15), with $\ell = 10$ km inside the fault zone and ℓ in the order of 150 km outside the fault zone. Gaebler et al. (2019) found similarly small scattering mean free path values along the northern strand of the NAFZ analyzing the energy decay of earthquake records with a central frequency of 0.75 Hz.

The first works considering non-uniform media are by Kanu and Snieder (2015a, 2015b), in which the authors modeled the wavefield by finite difference simulations to compute the energy density from the waveforms in

order to numerically compute the kernels. Recently, Zhang et al. (2021) modeled sensitivity kernels for elastic body waves in 2D random heterogeneous scattering media based on radiative transfer theory using a Monte Carlo approach. The authors use a similar probabilistic approach as is used in current study, but a different computation method. Furthermore, the scattering contrasts considered in current study are larger.

In this work we explore the impact of scattering distribution on coda wave sensitivity kernels for the acoustic scalar case. We show examples of sensitivity kernels for realistic settings, in which we consider large contrasts of scattering properties that are supported by seismic observations. Guided by the kernels obtained for volcanic and fault zone settings, we highlight the different sensitivities of three classical coda wave observables. In addition, the parametric part of this study (Section 4.2) aids in the understanding of the kernels.

2. Coda-Wave Sensitivity Kernels

When monitoring the subsurface, one aims to invert observations to gain information about the perturbation of medium properties. As the name suggests, the sensitivity kernels quantify the spatial and temporal sensitivity of a specific observable to changes in the medium. The kernels facilitate the reconstruction in 2D or 3D of the spatial variation of a given physical parameter, such as the wave speed or scattering properties. Since different observations require the use of different kernels, we compute three types of sensitivity kernels: the travel time kernel K_{tt}, the scattering kernel K_{sc}, and the decorrelation kernel K_{dc}.

The travel-time kernel, K_{tt}, relates the observed travel-time delay (or phase shifts) between coda waves for different recording periods to perturbations in propagation velocities. In this study we use the kernel as defined by Margerin et al. (2016) and Mayor et al. (2014):

$$K_{tt}(\mathbf{r}',\, t;\mathbf{r},\, \mathbf{r}_0) = S^D \int_0^t \int_{S^D} \frac{I(\mathbf{r}',\, t-t',\, -\mathbf{n}';\mathbf{r}) I(\mathbf{r}',\, t',\, \mathbf{n}';\mathbf{r}_0) dt' d\mathbf{n}'}{I(\mathbf{r}, t;\mathbf{r}_0)} \tag{1}$$

where a forward-backward formalism is employed in which the receiver is placed on an equal footing as the actual source. The intensity propagators I are based on the 2D radiative transfer equation (RTE; Paasschens, 1997; Sato, 1993), and depend on $\mathbf{r}_0$, $\mathbf{r}$, and/or $\mathbf{r}'$, which corresponds to the position vectors for the source of forward intensity, the source of backward intensity and the perturbation, respectively. $\mathbf{n}'$ is an unit vector indicating the propagation direction and S^D denotes the unit sphere in space dimension D, as well as its area. The intensity in the denominator of Equation 1 is a *mean* intensity, which is the angular average intensity, and can also be described as the energy density stored in a certain volume or surface. On the other hand, the numerator of Equation 1 is a convolution between *specific* intensities of two sources: one source of forward intensity and one of backward intensity. The specific intensity is a directionally dependent intensity, defined as the amount of energy flowing around direction $\mathbf{n}'$, through a small surface element dS located at point $\mathbf{r}$ and at a certain time t within a defined frequency band (e.g., Margerin, 2005).

Note that the intensity, or energy density, has dimension $[L]^{-D}$ (Paasschens, 1997) so that the kernel has dimension $[t][L]^{-D}$. The kernel is a time density equal to the time spent by the waves around a given point, per unit volume or surface. The kernel is valid for anisotropic scattering, although we consider only isotropic scattering in current work. Previously, Mayor et al. (2014) introduced a similar sensitivity kernel for the perturbation of intensity caused by a local change in absorption. In Margerin et al. (2016) this sensitivity kernel is reinterpreted probabilistically as the travel-time kernel.

Of a different nature are small structural changes in the subsurface, for example, the growth of a fault, resulting in a perturbation of scattering. An extra scatterer creates new propagation paths for the waves, which in turn slightly modifies the coda signal. As a consequence, one can observe a decorrelation of the waveform in the recordings for different periods of time (Planès et al., 2014). The decorrelation kernel, K_{dc}, relates this observation to the local change in scattering of the medium. The kernel takes into account the new propagation paths that have been created by the addition of scatterers, and is defined as follows (Margerin et al., 2016; Planès et al., 2014):

$$K_{dc}(\mathbf{r}', t;\mathbf{r},\mathbf{r}_0) = \int_0^t \frac{I(\mathbf{r}', t-t';\mathbf{r}) I(\mathbf{r}, t';\mathbf{r}_0) dt'}{I(\mathbf{r}, t;\mathbf{r}_0)} \tag{2}$$

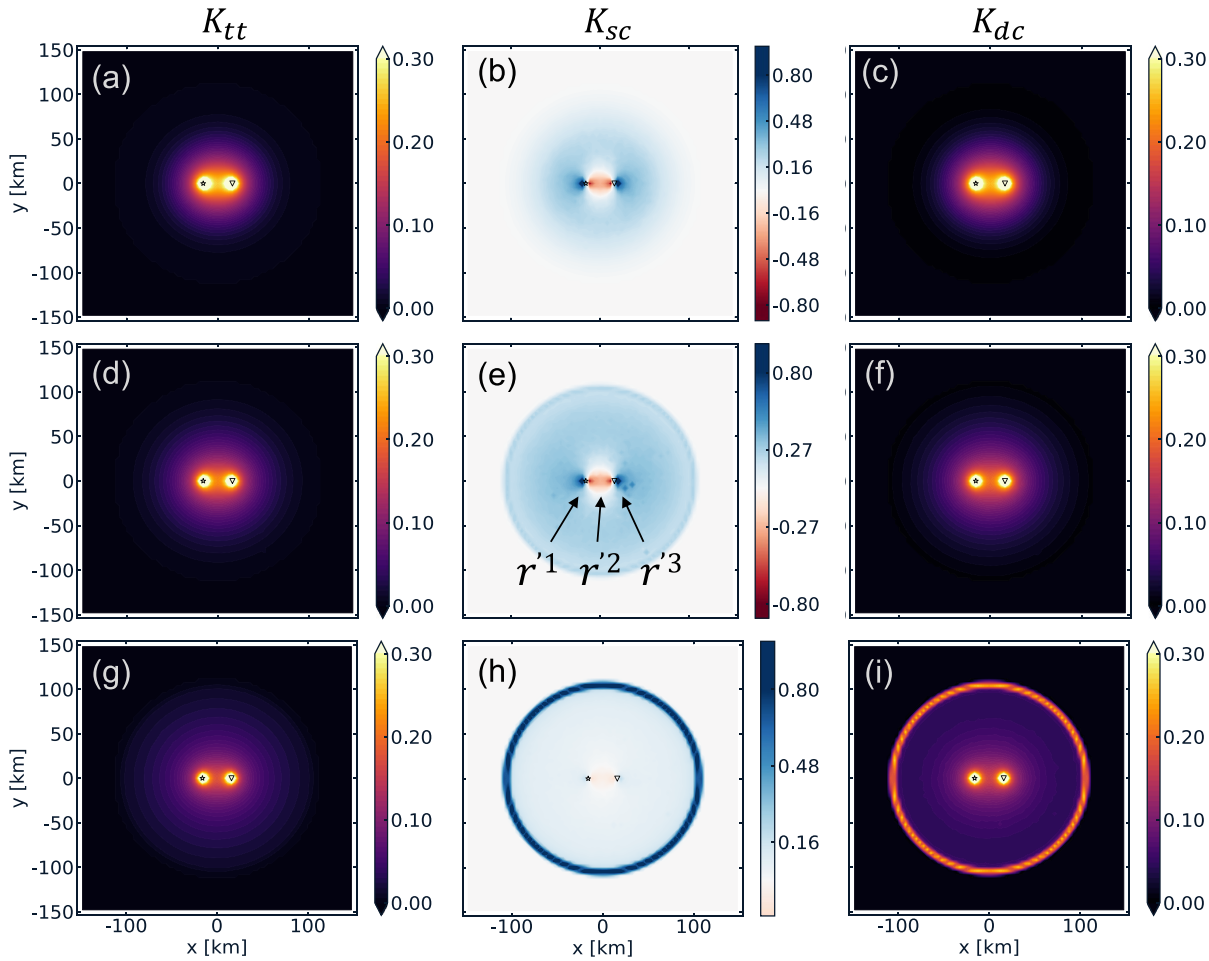

Figure 1. Sensitivity kernels for uniform scattering media at 100 s lapse-time. The columns show K_{tt} ((a), (d), (g)), K_{sc} ((b), (e), (h)) and K_{dc} ((c), (f), (i)), respectively. The scattering mean free path increases from top to bottom: ℓ_1, $2 \times \ell_1$, $8 \times \ell_1$, with $\ell_1 = 30$ km. The inter-source distance is 32 km. The annotations $r'^1 - r'^3$ point to positive, negative, and positive sensitivity along the line connecting the sources, respectively. All kernels are normalized with respect to the maximum value. *Note*. That for K_{sc} the color bar is symmetric around zero, with red as negative and blue as positive sensitivities, respectively.

All the intensities in Equation 2 are *mean* intensities, therefore the decorrelation kernel is dependent on the mean energy densities only and not on the directivity of the intensities, implied by the absence of the directivity dependence of the energy propagation ($\mathbf{n}'$). Note that Equation 2 is valid *stricto sensu* in the case where the structural change behaves as an isotropic scatterer. In the scalar approximation employed in this work, this implies that they are small compared to the probing wavelength. We emphasize that the scattering properties of the reference medium may be completely arbitrary. Another observation for the same medium change, that is, the scattering perturbation, is a change in relative intensity $\delta I/I$. Since the observation is different than in the case of the decorrelation, one needs another sensitivity kernel. Physically, a perturbation in scattering located in a volume $\mathrm{d}V(\mathbf{r}')$ has two effects on the intensity. (a) An energy loss, which can be quantified by evaluating the extra-attenuation of seismic phonons that cross $\mathrm{d}V(\mathbf{r}')$. This contribution is effectively quantified by K_{tt}. (b) An increased probability of energy reaching the detector due to the additional paths created by the additional scatterer. This is effectively what K_{dc} provides us with. Therefore, the scattering sensitivity kernel K_{sc}, as derived by Mayor et al. (2014), is defined as:

$$K_{sc}(\mathbf{r}', t; \mathbf{r}, \mathbf{r}_0) = K_{dc}(\mathbf{r}', t; \mathbf{r}, \mathbf{r}_0) - K_{tt}(\mathbf{r}', t; \mathbf{r}, \mathbf{r}_0) \tag{3}$$

Note that the scattering pattern of the new scatterers should be isotropic implying as above that they are small compared to the wavelength. A characteristic of this kernel is that the integral over all detection points $\mathbf{r}$ gives 0, implied by the conservation of energy as demonstrated in the work of Mayor et al. (2014). We will also find in the results (e.g., Figure 1) that the scattering kernels have both positive and negative sensitivities to scattering

perturbations. In other words, the spatial distribution of intensities is modified while the total intensities remain unchanged. For an extension of Equations 1–3 to coupled *P* and *S* waves (see Zhang et al., 2021)

3. Computation of Sensitivity Kernels

In this section, we provide an overview of the different approaches that have been employed in the literature to compute the sensitivity kernels defined in Equations 1–3. We will begin by discussing techniques that are based on the direct computation of the convolution integrals. These methods require the global computation of the time-dependent intensity at every point of the target medium. A first way to get access to the spatio-temporal distribution of intensity in a scattering medium is to perform full wavefield simulations in a series of realizations of randomly perturbed media with prescribed statistics. An ensemble average can be subsequently performed to smooth out the fluctuations of the intensity. The advantage of the full wavefield approach is that the coupling between all types of waves, including surface waves, is incorporated in the modeling. Furthermore, spatial variations of propagation properties can be easily implemented. Kanu and Snieder (2015a) considered the effect of non uniform properties on the spatio-temporal dependence of sensitivity kernels. They performed finite difference simulations in complex 2-D acoustic media including spatial variations in both background velocities and correlation function of the random medium. Their study provides a clear illustration of the impact of spatially varying scattering properties on the spatio-temporal dependence of sensitivity kernels. Duran et al. (2020) developed the theory of decorrelation kernels for coupled elastic waves. In their formulation the sensitivity is decomposed onto a *P*–*S* polarization basis. To compute the *P* and *S* intensities in a scattering medium, they apply the Helmholtz decomposition to full wavefield simulations in inhomogeneous media. Their theory is carefully validated through a series of numerical experiments where the effect of adding a single scatterer at different positions is investigated. These authors report excellent agreement between theory and synthetic data. A hybrid method combining analytical and full wavefield approaches was adopted by Obermann, Planès, Larose, and Campillo (2013). These authors studied more particularly the relative contributions of surface and body waves in the coda. They proposed to express the traveltime sensitivity kernel of coda waves as a linear combination of surface and body waves kernels, that have been determined theoretically without coupling. To take into account the energy exchange between the two types of waves, the coefficients of the linear combination are allowed to depend on the lapse-time and are determined through numerical simulations in a heterogeneous 2-D elastic half-space. The approach of Obermann, Planès, Larose, and Campillo (2013) reproduces well the main features of the coda sensitivity seen in the numerical simulations. An extension to a 3-D elastic half-space was presented in Obermann et al. (2016). The examples cited above illustrate the great flexibility of full wavefield simulations. We note, however, that this approach suffers from an important drawback. Indeed, Equations 1 and 3 show that the specific intensity (and not its angular average) is required to compute the travel-time and scattering sensitivity kernel. This point has not been addressed in the full wavefield approach so far. It is only in the diffusion regime (i.e., after sufficiently many scattering events) and at sufficiently large distance from the source that it is appropriate to approximate the specific intensity by its angular average. But even so, such an approximation may lead to unphysical results. As an obvious example, if one replaces the specific intensity by its mean value in Equation 3, one arrives at the conclusion that the sensitivity of the intensity to a local change in scattering properties is 0, which is clearly incorrect.

Because radiative transfer theory underpins the derivation of sensitivity kernels, this theory is a natural candidate for their computation. The key difficulty in the evaluation of the convolutions in Equations 1–3 is the calculation of global fundamental solutions (or Green's functions) of the RTE. Standard quadrature schemes may subsequently be employed to carry out the integrations numerically. Mayor et al. (2014) employed analytical solutions developed by Paasschens (1997) for isotropic scattering of scalar waves in 2D. In applications to real data, the isotropy assumption can be limiting. To take non-isotropic scattering into account Margerin et al. (2016) introduced a spectral method based on a Fourier-Bessel series for the specific intensity. To cope with the strong anisotropy of the intensity in the vicinity of the source, these authors treated analytically the coherent and single-scattering intensity. The methods cited thus far are limited to statistically uniform media with constant background velocity. Zhang et al. (2021) extended the sensitivity kernel theory to the case of coupled elastic *P* and *S* waves in laterally varying media. In numerical applications, they considered the case of objects exhibiting a contrast of scattering/absorption properties w.r.t. a statistically uniform background in 2D elastic full-space. To evaluate the kernels, they employed Monte Carlo simulations to compute an angularly discretized version of the time-dependent *P* and *S* specific intensities on a grid of points covering the target medium. A similar approach

was employed by Sens-Schönfelder et al. (2021) to compute the sensitivity of high-frequency scattered body wave phases to scattering perturbations located in the deep mantle. Their study highlights nicely the regions of the deep Earth contributing to the generation of precursors to the PKP phase. These recent results illustrate well the versatility of Monte-Carlo methods.

Independent of the mathematical derivation of sensitivity kernels, Monte-Carlo methods have been employed for a long time in for example, nuclear engineering to compute the sensitivity of observables to perturbations in scattering/absorption properties. In this approach, which is often referred to as "differential Monte-Carlo method" in the literature, the sensitivities are computed "on the fly" as the energy propagates from the source to the receiver (Lux & Koblinger, 1991). The differential Monte-Carlo method was introduced for elastic waves by Takeuchi (2016) to compute the sensitivity of teleseismic waves and their coda to perturbations of scattering and absorption properties at depth in the Earth. In this example, the kernels are discretized onto layers where the scattering/absorption properties may be perturbed independently. The approach we adopt in the present work also belongs to the family of differential methods. The twist that differentiates it from previous works is the introduction of the method of delta (or null) collision in the Monte-Carlo algorithm to treat spatially variable scattering/absorption properties. The technique is described in details in Appendix A but we summarize briefly its main features here. In effect, our method replaces a medium where attenuation varies spatially with a medium where attenuation is uniform by introducing fictitious scattering events that do not modify the direction of propagation of the waves (hence the names null or delta collision). As detailed in Appendix A, an important consequence of this approach is that it requires absolutely no particle tracking effort. This property considerably simplifies the algorithm and allows for a simple treatment of media with completely arbitrary spatial variations of scattering/absorption properties. In this work, we will particularly focus on high-contrast geological objects such as volcanoes or fault zones.

4. Sensitivity Kernels for Non-Uniform Scattering Media

In this section we discuss the effect of the scattering distribution on the sensitivity kernels. Guided by the results obtained in a volcanic setting, we introduce the physical interpretation for each of the three different kernels. The second context for which we investigate the implications of non-uniform scattering strength on the sensitivities is for a model with two half-spaces. This case is illustrated with the aid of two parametric studies, which facilitate the interpretation of the kernels. We will finish this section with an application to a fault zone model.

To facilitate the discussion we compare the results for all three non-uniform models to the kernels for uniform media. The latter are shown in Figure 1 at a lapse-time of 100 s for increasing scattering strengths. The columns from left to right show K_{tt}, K_{sc}, and K_{dc}, respectively. The results obtained for a reference medium, with $\ell_1 = 30$ km, is shown at the top row. The scattering mean free path varies over orders of magnitude in the Earth, therefore we compare the reference medium with weaker scattering media. The middle and lower rows of Figure 1 show the results for increasing ℓ: $2 \times \ell_1$ and $8 \times \ell_1$, respectively. The epicentral distance is set to $R = 32$ km. The numerical results shown in Figure 1 will serve as guides to understand the more complex cases associated to non-uniform scattering properties.

4.1. Volcanic Setting

Figure 2 shows the kernels for a source and detector that are 47 km apart, at 40 s (upper row) and 80 s (lower row) lapse-times, in the vicinity of a volcano. The volcano, characterized by strong scattering, has a scattering mean free path of 2 km and a radius of 6 km. These values are based on the findings of Hirose et al. (2019) at the Sakurajima volcano in Japan. The surrounding crust has a weaker scattering strength with $\ell = 150$ km, and for simplicity the intrinsic absorption is considered uniform with $Q_i = 100$.

A couple of observations stand out from Figure 2. First, the travel-time and decorrelation kernels are very dissimilar. Second, the volcano appears to be a reflector for the intensities at early lapse-times. To explain these observations and improve the understanding of the kernels we will discuss all three kernels separately and compare them to the uniform model as reference, starting with the travel-time kernel, then the decorrelation kernel and finally the scattering kernel.

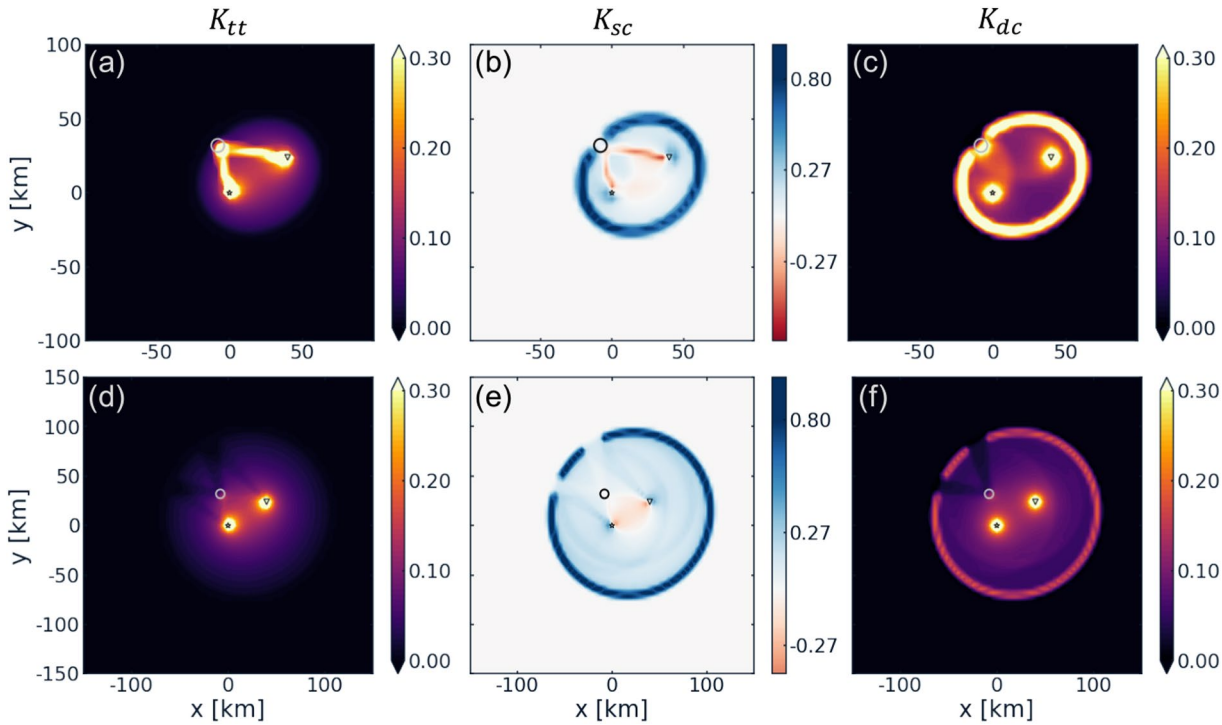

Figure 2. Sensitivity kernels for volcanic setting, for lapse-time of 40 s ((a)–(c)) and 80 s ((d)–(f)). The columns show K_{tt}, K_{sc}, and K_{dc}, respectively. The volcano is depicted as a circle with radius 6 km and $\ell_v = 2$ km, outside the volcano $\ell = 150$ km. The inter-source distance is approximately 47 km. *Note*. That axis extent is not the same for 40 s (±100 km) and 80 s (±150 km). All kernels are normalized with respect to the maximum value. The color bar for K_{sc} is symmetric around zero.

As defined in Equation 1, K_{tt} is dependent on the dominant propagation direction of the waves. There are two specific intensities contributing to the travel-time kernel, coming from two different primary sources: (a) the forward intensity, I_s, from the source toward the perturbation; and (b) the backward intensity, I_d, from detector toward the perturbation. In the application part of this manuscript we refer to the first source as the "source of forward intensity" or "forward source," while the latter will be referred to as the "source of backward intensity" or "backward source" from hereafter.

Where the forward and backward intensities are simultaneously high and propagating in opposite direction, the travel-time kernel shows high sensitivities, as dictated by the convolution of specific intensities in the numerator of Equation 1. In the uniform case, there are only two sources to be considered I_s and I_d. In the case of a localized perturbation with high scattering contrast, energy may be back-scattered by the heterogeneity, giving rise to a secondary and delayed intensity $I_{s,d}^{\Delta\ell}$. An overview of the different intensities is presented in Table 1.

Table 1
Overview of Intensities and Fluxes

Symbol	Description
I_s	Intensity from the source: Forward intensity
I_d	Intensity from the detector: Backward intensity
$I_{s,d}^{b}$	Intensity along the ballistic path between source and detector
$I_{s,d}^{\Delta\ell}$	Secondary and delayed intensity induced by a strong scattering region
$\mathbf{J}_s$	Energy flux from the source
$\mathbf{J}_d$	Energy flux from the detector
$\mathbf{J}_{s,d}^{b}$	Energy flux along the ballistic path between source and detector
$\mathbf{J}_{s,d}^{\Delta\ell}$	Secondary and delayed energy flux induced by a strong scattering region

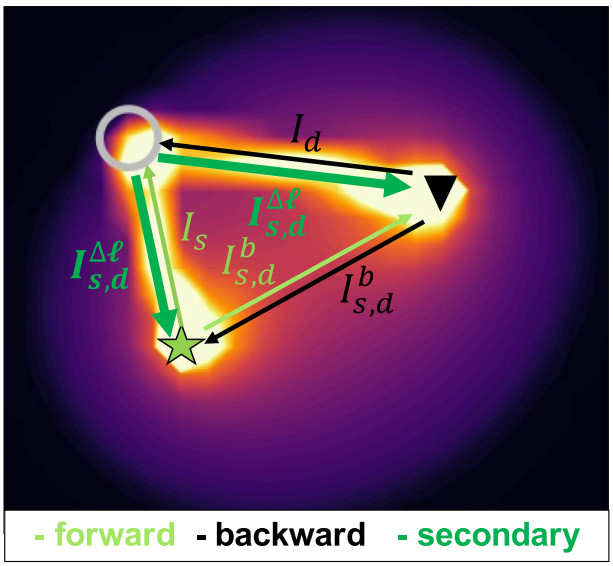

Figure 3. Depiction of the specific intensities controlling K_{tt} in a volcanic setting. The green star depicts the source and the black triangle the detector. The former and the latter are referred to as source of forward and source of backward intensity, respectively. The gray circle shows the location of the volcano. Specific intensity I_s (I_d) propagates from the source of forward intensity (source of backward intensity) to the volcano, respectively. Back-scattered energy is indicated as $I^{\Delta\ell}$. It originates from one source and propagates via the volcano to the other source (and vice versa), but it also has an energy contribution coming from one source that scatters back to the same source. Both sources emit intensities into all directions, also on the direct path between them, as indicated by I_s and I_d.

The key intensities for the volcanic setting are shown in Figure 3. As a result of the highly scattering volcano, specific intensities propagate from the forward source toward the volcano (I_s, in light green), and scatter from the volcano to the source of backward intensity ($I^{\Delta\ell}_{s,d}$, in dark green). Similarly, intensities propagate from the source of backward intensity to the volcano (I_d, in black) and from the volcano to the forward source ($I^{\Delta\ell}_{s,d}$, in dark green). For 40 s lapse-time, we can therefore explain the high sensitivities on the paths connecting the sources via the volcano, by the high specific intensities that are opposite in direction on those paths. For the uniform case we observe higher sensitivities around and between the sources, especially for strong scattering media the sensitivity on the direct path between the sources increases (Figure 1a). This direct path is less favorable in the volcanic setting, because the specific intensities are much higher on the paths that connect the sources of forward and backward intensity via the volcano. In other words, for early lapse-times the volcano acts as a secondary and delayed source of intensity and therefore promotes an additional path favorable to energy transport between the primary sources, which is not present in the uniform case. For later lapse-time (80 s; Figure 2d), K_{tt} resembles its equivalent for a uniform medium. Yet the imprint of the volcano remains as the strongly scattering zone prevents ballistic energy to travel through and causes a "shadow" in the kernel for late lapse-times. The partly removed ballistic energies originating from both sources cause an "M"-shaped shadow to appear, which deforms and gradually disappears with lapse-time. At later lapse-times the effect of the volcano starts to disappear as the portion of multiply scattered energy increases, resulting in a probability increase for two specific intensities to propagate in opposite directions in these areas. Animations of the three different kernels with increasing lapse-time for the volcanic setting can be found in the Supporting Information, Movies S1–S3.

The decorrelation kernels appear rather different from their travel-time counterparts. Indeed, Equation 2 shows that K_{dc} does not depend on the specific intensities, but on the mean intensities instead. The decorrelation kernel will thus be high where the mean intensities emitted by the forward and backward sources are simultaneously high. This condition is far less stringent than the analogous one for the travel-time kernel. For this reason the travel-time and decorrelation kernel are dissimilar. The K_{dc} for the volcanic case at early lapse-time (40 s; Figure 2c) shows high sensitivity around the sources and on the single scattering ellipse. Additionally, high sensitivity can be observed in the halos surrounding the forward source and volcano, and the backward source and volcano, respectively. Energy becomes rapidly diffuse when it enters into the volcano, therefore the high intensities inside the volcano are on the side that faces the sources; hence a bend in the single scattering ellipse can be observed (Figure 2c). For later lapse-times (80 s; Figure 2f), K_{dc} appears similar to the uniform K_{dc} (Figure 1i). Nevertheless, the imprint of the strongly scattering volcano remains, causing a shadow on the single-scattering ellipse of the decorrelation kernel.

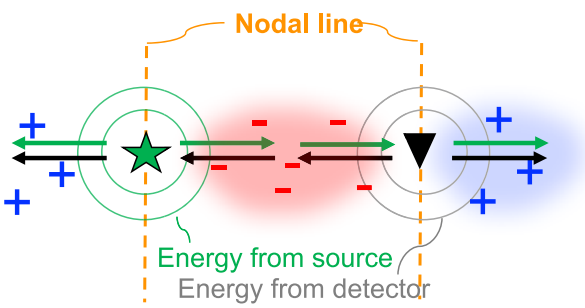

Figure 4. Graphical interpretation of the fluxes explaining the pattern of the scattering kernel for a uniform scattering medium. Energy from the source (green star) is emitted in all directions, indicated by the green circles. The green arrows depict the fluxes along the line connecting the source and detector. Similarly, energy from the detector (black triangle) is emitted in all directions, indicated by the gray circles. The black arrows depict fluxes from the detector in the source-detector line. In the space between source and detector the fluxes have opposite direction, resulting in negative sensitivity (red "−"). In the outside spaces, the fluxes from source and detector have similar directions, resulting in positive sensitivity to scattering (blue "+"). The nodal lines are depicted by the orange dashed line.

The last kernel to be considered is the scattering kernel (Figures 2b and 2e). In order to understand its structure in the vicinity of a volcano, we will first discuss the pattern of K_{sc} for the uniform case (e.g., Figure 1e). As mentioned in Section 2, the scattering kernel has positive and negative sensitivities. To describe the pattern of the scattering kernel intuitively, we imagine placing additional scatterers at three locations in Figure 4. If an extra scatterer would have been placed left of the forward intensity source, the chances of additional energy reaching the backward intensity source would have been increased due to the possibility of back-scattering. Due to reciprocity, this

same argument holds for an additional scatterer located right of the backward source. On the other hand, negative scattering sensitivity between the two sources indicates that if an additional scatterer would have been placed in the red area, the probability of energy coming from one source and reaching the other source would decrease.

In a more physical manner, the signs in the kernels can be understood in the following way. If we imagine point sources at the locations of the source and detector that inject energy into the medium at time $t = 0$. The energy transport gives rise to fluxes going from a source of forward intensity to a source of backward intensity (and vice versa). At late lapse-times, which is at several scattering mean free times τ (where $\tau = \ell/c$ with c as wave velocity), the energy is diffuse. Previously, it has been shown in the literature that in the diffusion regime the scattering kernel is controlled by the scalar product of the energy flux vectors $(\boldsymbol{J})$ for sources located at the position of the forward/backward intensity sources (e.g., Arridge, 1995; Mayor et al., 2014; Wilson & Adam, 1983):

$$\lim_{t\to+\infty} K_{\mathrm{sc}}(\mathbf{r};\mathbf{r}';\mathbf{r}_0;t) = D(1-g)\int_0^t \mathbf{J}_{\mathbf{fwd}}(\mathbf{r}';\mathbf{r};t-t')\cdot\mathbf{J}_{\mathbf{bwd}}(\mathbf{r}';\mathbf{r}_0;t')\mathrm{d}t' \tag{4}$$

with g denoting the mean cosine of the scattering angle. Note that Equation 4 is not strictly valid quantitatively, although qualitatively it is correct. Hence, Equation 4 is rather an approximate than an exact formula, which in practice explains the pattern of the scattering kernel accurately. It contains the essential physics and therefore we employ this formulation heuristically to analyze our results. We would like to emphasize that Equation 4 is used to understand the signs and relative magnitude of the scattering kernel. No diffusion approximation has been used to derive the kernel Equations 1–3. Figure 4 shows a schematic diagram of the fluxes in the scattering kernel for a uniform medium. The energy flux flows away in all directions from the source and similarly for the detector. On the direct path between source and detector, these fluxes have opposite direction while on the outside the fluxes have similar directions. As a consequence of the scalar product in Equation 4, the fluxes in opposite direction lead to an area of negative sensitivity to scattering on the direct path. Here, the probability of energy reaching the other source is decreased. On the outer side of the direct path between the sources, there is a positive sensitivity due to the scalar product of the fluxes in similar direction. In these positive areas the probability of energy reaching the other detector is increased. The line that divides the positive and the negative sensitivities in the vicinity of the source/detector is referred to as the nodal line (Figure 4).

Now that we have discussed the positive and negative signs in K_{sc} for a uniform medium we continue the discussion about the volcanic case. K_{sc} will be high in absolute value where the actual energy fluxes are simultaneously large and aligned, either parallel or anti-parallel. Consequently, an additional energy transport channel in the scattering kernel for early lapse-times (40 s; Figure 2b) appears as strong negative sensitivities, connecting the two sources via the volcano. The negative sensitivity on the direct path between the sources is also present, albeit weaker than on the path via the volcano. Similarly as for K_{tt}, this is due to smaller energy current vectors on the direct path. Furthermore, we can observe similarities between the decorrelation and the scattering kernel, for both the early and late lapse-times. In particular, the single scattering ellipse and the halos of high sensitivity between either source or volcano, which are also present in K_{dc}, can be observed in Figures 2b and 2e). Although K_{sc} for the volcanic setting at late lapse-time (80 s) resembles its equivalent for a uniform model, the effect of the volcano remains.

4.2. Two Half-Spaces Setting

In the northeastern region of Honshu, Japan, Yoshimoto et al. (2006) estimated the spatial distribution of attenuation. These authors found that the contrast of properties between the front-arc and the back-arc is approximately equal to two for both absorption and scattering. With this in mind, we explore the effect of non-uniform scattering properties on the coda wave sensitivities, in a medium composed of two half-spaces. A tectonic setting with a strike-slip fault that caused two different materials on each side of the fault to be in contact may also be considered in this context. For all half-space models, ℓ_1 is the smallest scattering mean free path we consider, it is kept constant at 30 km and consistently on the left side of the model. The right half-space has weaker scattering ($\ell_1 < \ell_2$), where ℓ_2 is chosen to differ by a factor of 2, 3, or 8 from ℓ_1. The interface delimiting the two half-spaces coincides exactly with the boundary between two pixels. d represents the distance from the forward intensity source to this interface.

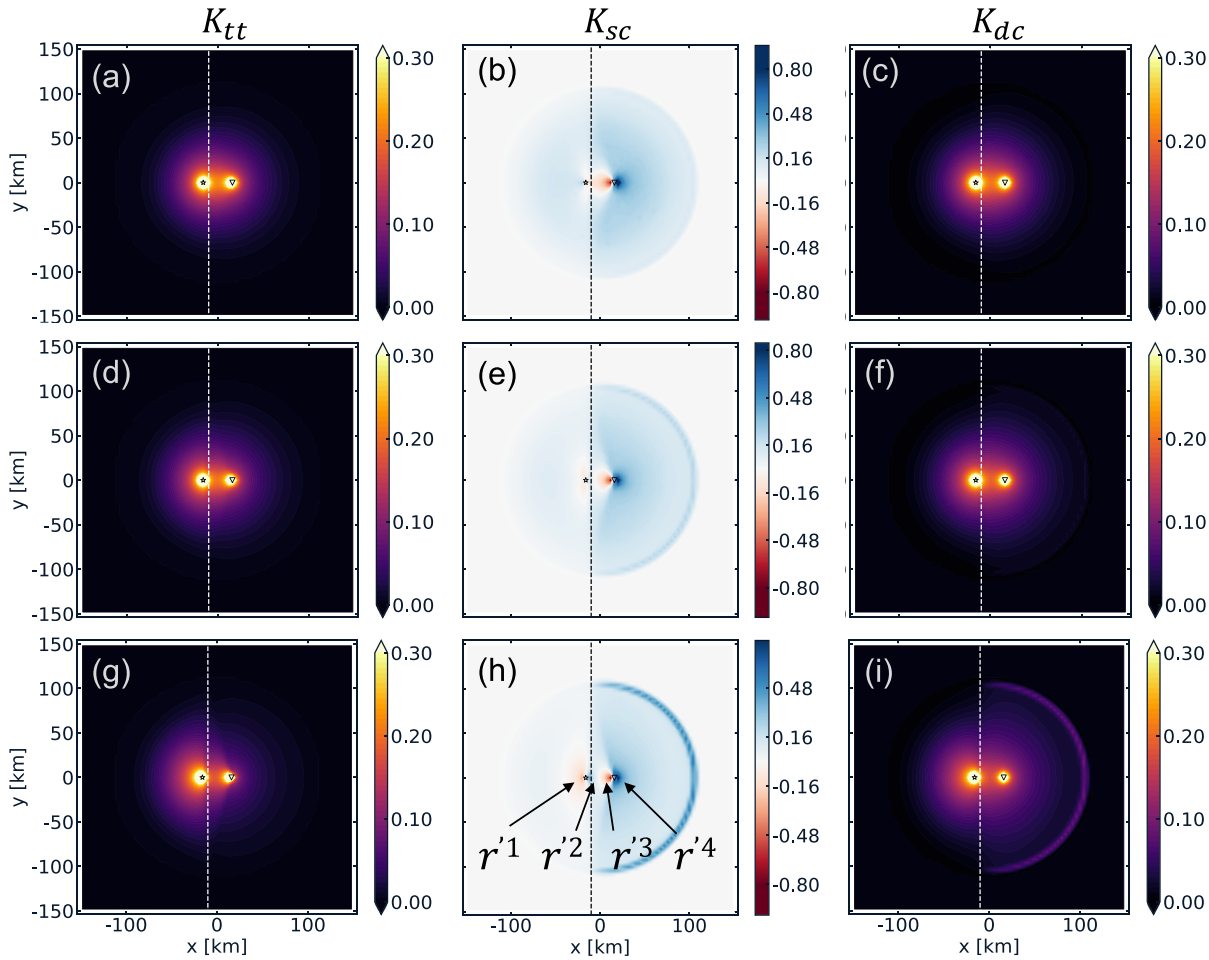

Figure 5. Sensitivity kernels for two half-spaces at 100 s lapse-time. The columns show K_{tt} ((a), (d), (g)), K_{sc} ((b), (e), (h)), and K_{dc} ((c), (f), (i)), respectively. The left half-space has a fixed scattering mean free path ℓ_1. The scattering mean free path in the right half-space increases from top to bottom: $2 \times \ell_1$, $3 \times \ell_1$, and $8 \times \ell_1$, with $\ell_1 = 30$ km. The source-detector distance R_0 is set to 32 km. The annotations $r'^1 r'^4$ point to negative, positive, negative, and positive sensitivity along the line connecting source and detector, respectively. All kernels are normalized with respect to the maximum value. Note. That for K_{sc} the color bar is symmetric around zero, with red as negative and blue as positive sensitivities, respectively.

The sensitivity kernels with sources in opposite half-spaces are shown in Figure 5, for $t = 100$ s. From the top to the bottom row, we show the results for increasing scattering contrast between ℓ_1 (the reference half-space, on the left) and ℓ_2 (the right half space): $\ell_2 = 2 \times \ell_1$ (upper), $\ell_2 = 3 \times \ell_1$ (middle), and $\ell_2 = 8 \times \ell_1$(lower). The dashed line, placed at 6 km from the source of forward intensity, depicts the boundary between the two half-spaces. The inter-source distance is the same as for the uniform cases, $R = 32$ km. We can observe that all three kernels for all degrees of scattering contrast are asymmetric, with the asymmetry intensifying as the contrast between ℓ_1 and ℓ_2 increases. In the travel-time kernel there is a strong effect of back-scattering, especially for the case where $\frac{\ell_2}{\ell_1} = 8$ (Figure 5g). The sensitivities appear higher in the strong scattering half-space. For the decorrelation kernels we can observe the increased difference between dominant transport regimes for increasing scattering contrasts. For example, in Figure 5i the dominant regime of wave propagation in the left half-space is diffusion. Therefore, the mean intensity and thus the sensitivity is spread over a larger area around the source. However, in the right half-space the propagation regime is essentially ballistic, consequently, strong sensitivities can be observed on the single scattering ellipse. The most striking observation from Figure 5 is the "flipped" pattern in the scattering kernels (w.r.t. the pattern for the uniform case), for $\frac{\ell_2}{\ell_1} \geq 3$ (Figures 5e and 5h). In the strong scattering half-space (with ℓ_1), the sensitivity to an additional scatterer left of the source is negative (r'^1 in Figure 5h), while it was positive for the uniform case (Figure 1e). On the other side of the source (r'^2) it is positive, while for the uniform case it was negative. The sensitivity to an additional scatterer in the weaker scattering half-space (with

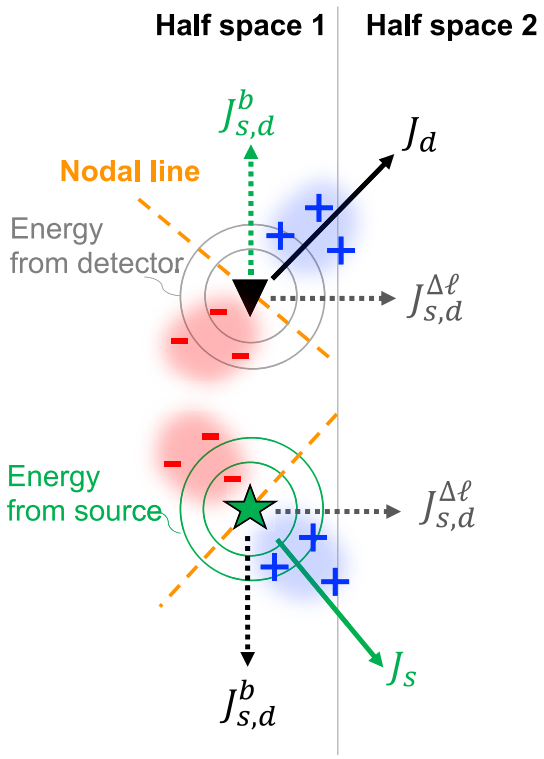

Figure 6. Graphical representation of the active fluxes and K_{sc} in case of a medium with two half-spaces. The fluxes shown in green are from the source of forward intensity. The flux $\mathbf{J}^{b}_{s,d}$ in green (black) is the part of the energy from the forward source (backward source) in the direction of the backward source (forward source), respectively. The resulting flux at the forward source, $\mathbf{J}_s$ shown in green, (backward source, $\mathbf{J}_d$ shown in black) has contributions from $\mathbf{J}^{b}_{s,d}$ and $\mathbf{J}^{\Delta\ell}_{s,d}$, respectively. $\mathbf{J}^{\Delta\ell}_{s,d}$ is the flux induced by the contrast in scattering. The nodal line, depicted in orange, separates positive and negative sensitivity to scattering and is perpendicular to the resulting energy flux.

ℓ_2) appears similar to that for the uniform case in the vicinity of the source, with negative sensitivity at r'^3 and positive at r'^4, regardless of the scattering strength or contrast.

Figure 5 shows that for a certain scattering contrast, the pattern of the scattering kernel changes significantly w.r.t. the uniform kernel. As explained for the volcanic setting, this is due to the active fluxes: from the forward source, $\mathbf{J}_s$, and the backward source, $\mathbf{J}_d$, but also the flux governed by the contrast in scattering $\mathbf{J}^{\Delta\ell}_{s,d}$. In order to improve our understanding of the "flipped" scattering kernel for models with two half-spaces and to gain more insight into the factors that affect the active fluxes we start by analyzing all fluxes separately (Figure 6), followed by two additional sets of simulations. In one set we take four models in which the scattering distribution of the medium is fixed, but the location of one of the sources rotates (Figure 7). In another set of simulations we investigate the effect of several parameters on the magnitude and directivity of each flux (Figure 8).

If we denote the part of $\mathbf{J}_s$ ($\mathbf{J}_d$) flowing in the direction of the backward source (forward source), respectively, as the direct flux $\mathbf{J}^{b}_{s,d}$. Then the flux at the sources is a combination of $\mathbf{J}^{b}_{s,d}$ and $\mathbf{J}^{\Delta\ell}_{s,d}$, as illustrated in Figure 6. For the situation in Figure 6, the magnitude of $\mathbf{J}^{\Delta\ell}_{s,d}$ depends on the contrast of scattering between both half-spaces. The orientation of $\mathbf{J}^{\Delta\ell}_{s,d}$ is perpendicular to the boundary of scattering and is directed from the stronger scattering half-space toward the weaker scattering half-space. The orientation of $\mathbf{J}^{b}_{s,d}$ depends on the positions of the sources, while its magnitude depends on the inter-source distance and lapse-time.

Figure 7 demonstrates how the direct flux and the flux induced by the scattering contrast contribute to the pattern of the scattering kernel. In all four panels the scattering contrast is fixed, with $\frac{\ell_2}{\ell_1} = 8$, and the orientation of $\mathbf{J}^{\Delta\ell}_{s,d}$ is perpendicular to the scattering boundary. From Figure 7a–7d the location of the upper source changes, but its distance to the lower source is kept constant at $R = 64$ km ($2 \times R_0$). We rotate the line connecting the two sources from parallel to the boundary (Figure 7a) to perpendicular to the boundary (Figure 7d). This causes the orientation of $\mathbf{J}^{b}_{s,d}$ to rotate and therefore the kernel pattern to change from a "twisted" version of the uniform kernel (Figures 6 and 7a) to a kernel with completely opposite sensitivity in the stronger scattering half-space (w.r.t. the uniform kernel), as we have already seen in Figure 5h.

There are multiple parameters that affect either direction or amplitude of $\mathbf{J}^{b}_{s,d}$, $\mathbf{J}^{\Delta\ell}_{s,d}$, and/or the relative contribution of both fluxes and therefore the kernels; a selection is shown in Figure 8. The effect of scattering contrast, and as a consequence on $\mathbf{J}^{\Delta\ell}_{s,d}$, can be seen when comparing Figure 8a where $\ell_2 = 2 \times \ell_1$ with Figure 8b where $\ell_2 = 8 \times \ell_1$. If ℓ_2 in the right half-space increases from $2\ell_1$ (Figure 8a) to $8\ell_1$ (Figure 8a) the kernel looks more asymmetric. Not only is the sensitivity partly focused on the single-scattering ellipse for the weaker scattering half-space, but also in the vicinity of both sources we observe a deformation of the kernel w.r.t. the uniform case. The angle γ, between the half-space boundary and the nodal line, decreases. Note that the nodal line is always perpendicular to the resulting flux at the source, as show in Figures 4 and 6. The change in γ is due to the larger $\mathbf{J}^{\Delta\ell}_{s,d}$, which is induced by the increasing scattering contrast. This alters the magnitude and direction of the flux, despite the unchanged orientation of the individual fluxes $\mathbf{J}^{\Delta\ell}_{s,d}$ and $\mathbf{J}^{b}_{s,d}$. Another parameter that affects the pattern of K_{sc} is the inter-source distance, which directly affects the contribution of $\mathbf{J}^{b}_{s,d}$ to the flux. For a larger R the angle γ increases as can be observed when comparing the kernel for $R = R_0$ (panel b) to $R = 3 \times R_0$ (Figure 8c).

Additionally, when comparing Figures 8b–8d we observe that the distance of the sources to the boundary of scattering contrast, d, also plays an important role in the pattern of the kernel. The kernel for larger d (Figure 8d) appears more similar to the kernel for uniform scattering (e.g., Figure 1) than the kernel for smaller d (Figure 8b). Thus the effect of the non-uniformity decreases with increasing d. The lack of sensitivity on the single-scattering

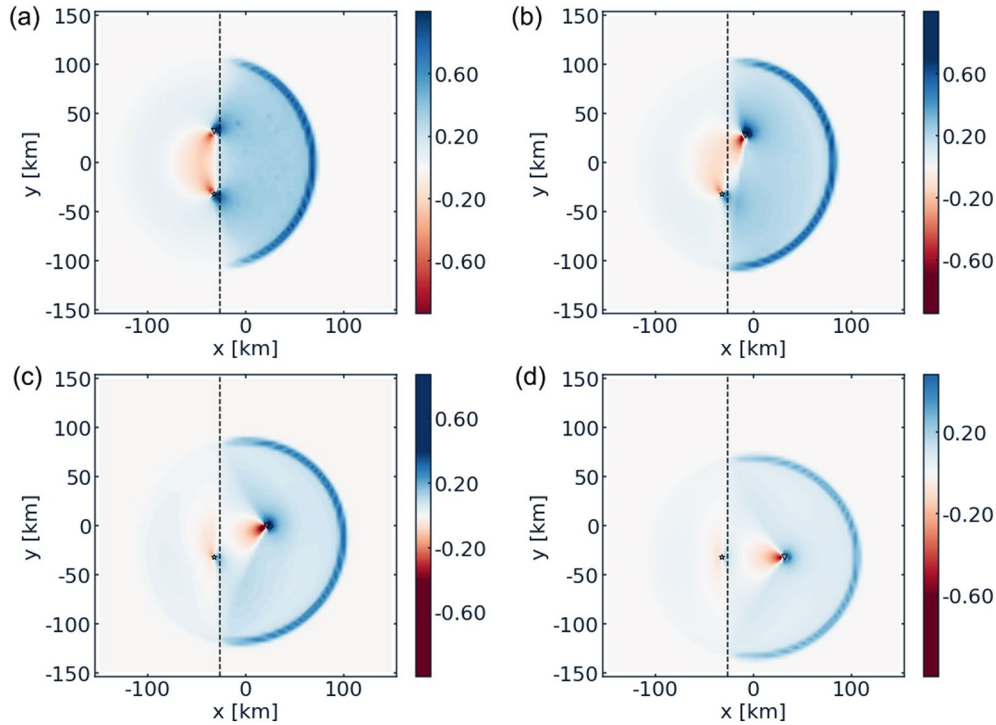

Figure 7. Sensitivity kernels for a half-space setting at 100 s lapse-time. The scattering mean free path for the left (right) half-space is fixed for all panels at ℓ_1 ($8 \times \ell_1$), respectively. The orientation of the line connecting the sources changes gradually from parallel to the boundary to perpendicular to the boundary, from (a) to (d), respectively. To enhance visibility of the kernel pattern the inter-source distance is larger, with $R = 2 \times R_0$. The distance of the leftmost source from the boundary is fixed at 6 km.

ellipse (Figure 8d) is a consequence of the energy being already diffuse before reaching the weaker scattering half-space. The two tests discussed above show that we can improve our interpretation of the scattering kernels by understanding the actual fluxes.

Finally, Figure 9 shows the effect of non-uniform scattering strength on the decorrelation, travel-time and scattering kernels for a model with sources far away from a boundary of scattering contrast. The sources are placed at a large distance (58 and 90 km) from the contrast of scattering inside the weaker scattering half-space, where $\ell_1 = 30$ km and $\ell_2 = \ell_1 \times 8$ km. In the travel-time kernel (Figure 9a) the strong backscattering effect, caused by the contrast in scattering, results in a larger sensitivity toward the strong scattering half-space. This is due to the overlap of intensities from the sources, which go toward the left, with the reflected intensity from the half-space that goes to the right. This travel-time kernel is rather different from the travel-time kernel for the uniform case (Figure 1), where the sensitivity would have solely been around the two sources. The decorrelation kernel shows concentrated sensitivities on the single scattering ellipse, as we have seen in the uniform weakly scattering medium. The sensitivity on the single-scattering ellipse in the left half-space is lower due to the stronger diffusion of energy in this region. Furthermore, higher sensitivities between the boundary of scattering on the one hand and both sources on the other hand, can be explained by the increase of mean intensities in those areas. Figure 9b shows that the impact on the scattering kernel is also significant. The contribution of the specific intensities, as in the travel-time kernel, is clearly visible and results in strong negative sensitivities toward the stronger scattering half-space. Furthermore, we can observe the single scattering ellipse, as we have seen in the decorrelation kernels.

The results in Figure 9 thus show that even at large distance from a boundary of scattering contrast the effect of non-uniform scattering properties on the sensitivity kernels can be significant. It is therefore important to have knowledge about the distribution of scattering for a large area around one's area of interest, in order to locate changes of the subsurface correctly.

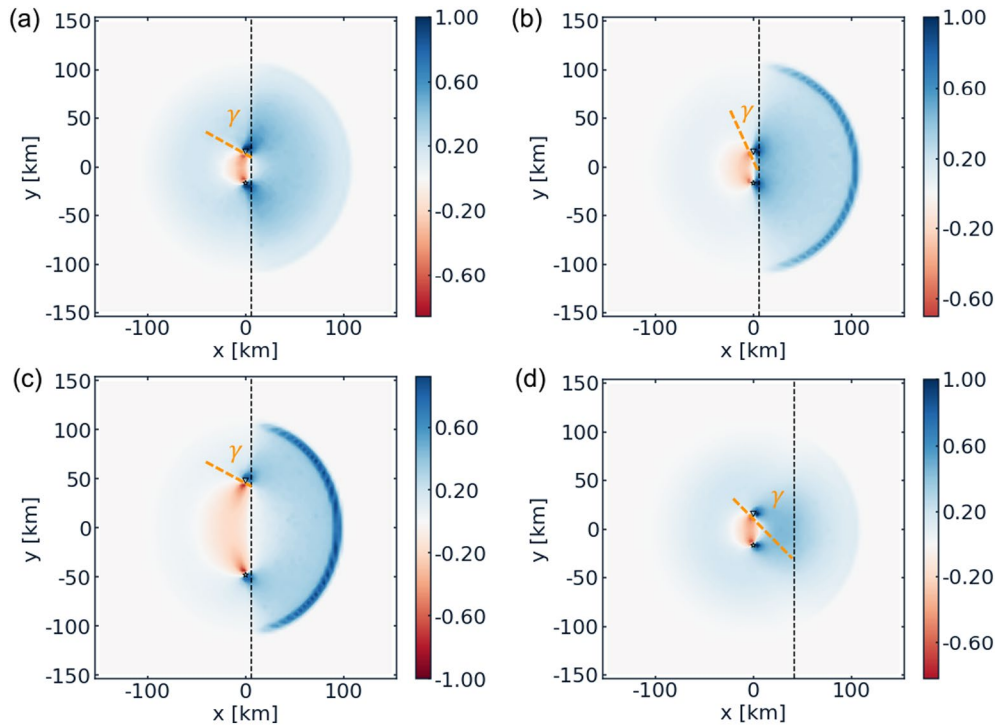

Figure 8. Sensitivity kernels for a half-space setting at 100 s lapse-time. Scattering mean free path of left half-space for all panels is $\ell_1 = 30$ km. Source and detector are placed parallel to half-space boundary. (a) ℓ of right half-space is $2 \times \ell_1$, $R = R_0 = 32$ km and distance to half-space boundary $d = 6$ km. (b) ℓ of right half-space is $8 \times \ell_1$, $R = R_0$, and $d = 6$ km. (c) ℓ of right half-space is $8 \times \ell_1$, $R = 3 \times R_0$, and $d = 6$ km. (d) ℓ of right half-space is $8 \times \ell_1$, $R = R_0$, and $d = 42$ km. γ denotes the angle between the nodal line (orange dashed line) and the half-space boundary. *Note*. That the color bar is symmetric around zero.

4.3. Fault Zone Setting

The last application we consider is a fault zone setting. The parameters are based on findings for the North Anatolian Fault (van Dinther et al., 2021). We consider a narrow fault zone of width = 6.25 km, with $\ell = 10$ km inside and $\ell = 150$ km outside. Figure 10 shows the resulting kernels for 65 s (upper) and 100 s (lower) lapse-times, respectively. Note that due to the inter-source distance of ~93 km in combination with a seismic velocity of 2.1 km s^{-1}, the earliest lapse-times for which the kernels are evaluated are around 45 s. The travel-time and scattering kernels may appear more complex than kernels shown for the other non-uniform media. In the travel-time kernel we observe two additional two-legged transport paths that connect the source and the detector. They are

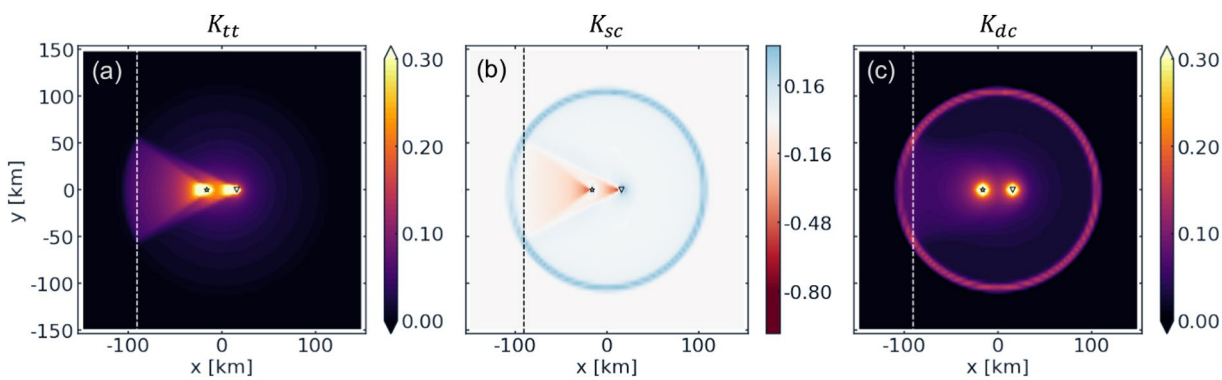

Figure 9. Sensitivity kernels for a model with two half-spaces at 100 s lapse-time, for a setting where the sources are far away from the boundary of scattering contrast (58 and 90 km, respectively). The scattering mean free path in the right half-space is $8 \times \ell_1$, where $\ell_1 = 30$ km. (a) shows K_{tt}, (b) K_{sc}, and (c) K_{dc}. All kernels are normalized with respect to the maximum value. The color bar for K_{sc} is symmetric around zero.

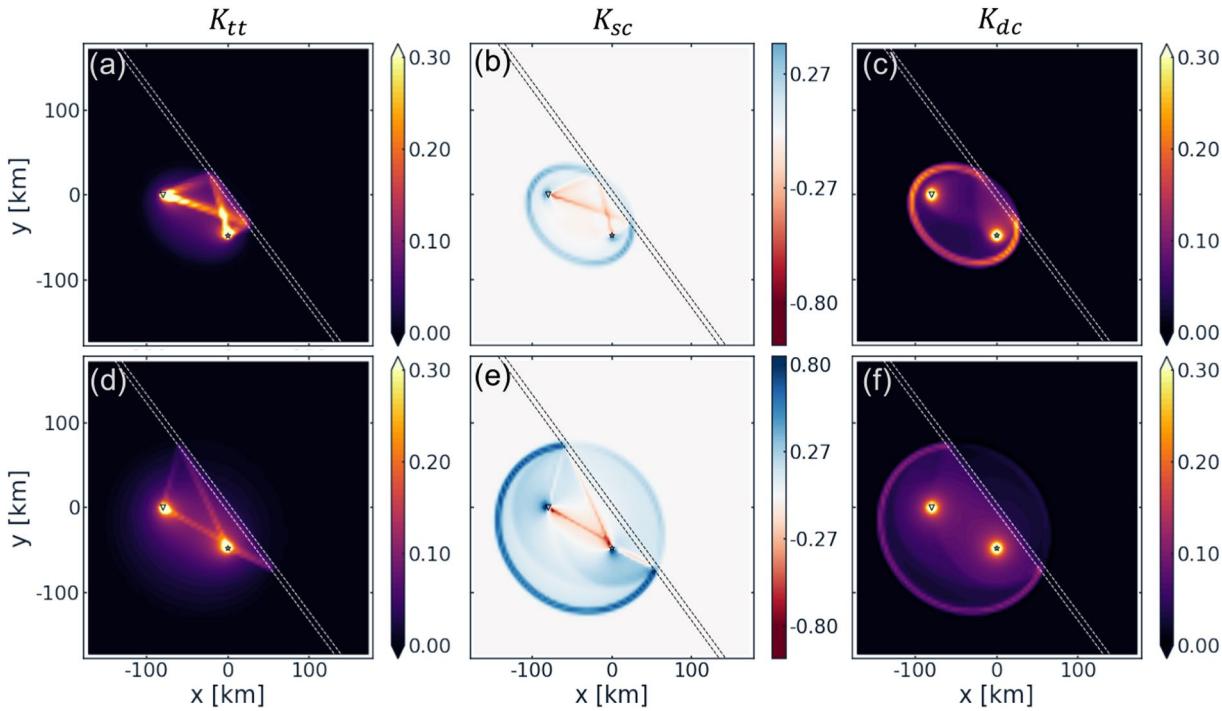

Figure 10. Sensitivity kernels for fault zone setting with both sources on one side of the fault (dashed lines), for lapse-times of 65 s (upper) and 100 s (lower). The columns show K_{tt} ((a)), (d)), K_{sc} ((b), (e)), and K_{dc} ((c), (f)), respectively. The width of the fault zone is 6.25 km. The scattering mean free path in and outside the fault zone are $\ell_{FZ} = 10$ km and $\ell = 150$ km, respectively. The distance between the two sources is ~93 km. All kernels are normalized with respect to the maximum value. The color bar for K_{sc} is symmetric around zero.

actually generated at the intersections of the single scattering ellipse with the fault zone where the strong scattering acts as secondary sources. For each of these paths, the backward and forward intensities are in exactly opposite directions. As explained for the K_{tt} of other models, the overlap of the specific intensities of either primary and/or secondary sources (in opposite direction) causes high sensitivities in the travel-time kernels. For the fault zone setting, this results in multiple pathways that are favorable for energy transport between the two primary sources (Figures 10a and 10d). For early lapse-time (65 s) we can observe a spot with even higher concentrated sensitivity, at the intersection of the energy transport paths. Furthermore, the geometry of these additional paths between the primary sources changes with lapse-time, as can be more clearly observed in the animations in the Supporting Information (Movie S4).

Figures 10b and 10e shows similar observations for the scattering kernel, where the simultaneously large and aligned energy fluxes create additional energy transport paths between the primary sources in the scattering kernel. The contribution of the high mean intensities is also visible in K_{sc}, which is similar to the halos of high sensitivities that are formed around the sources in the decorrelation kernel. Again K_{dc} does not resemble K_{tt}, and shows that the highly diffusive fault zone acts as a barrier for energy passing through. Hence, the mean intensity is low on the right side of the fault zone in Figure 10f. In the supporting information, additional animations for K_{sc} (Movie S5) and K_{dc} (Movie S6) with lapse-time for the fault zone setting can be found.

5. Concluding Remarks

For monitoring the temporal evolution of the subsurface we need coda wave sensitivity kernels that linearly relate observed changes in recordings to physical medium changes. Here, we compute travel-time, scattering, and decorrelation kernels based on a flexible Monte Carlo method, which enables us to include non-uniformly distributed scattering properties. In this work we have shown that non-uniform scattering properties can have a profound and non-intuitive effect on coda wave sensitivity kernels. Hence, it could be misleading to overlook the distribution of scattering properties in monitoring applications. The actual impact on the kernels depends on a combination of lapse-time and mean free time, it is therefore important to have knowledge about the geology and

an estimate on the scattering mean free path in the wider region that is targeted to be monitored. Lack of a good a priori scattering model may lead to a mislocation of the medium changes.

As previously put forward in theoretical studies (Margerin et al., 2016; Snieder et al., 2019; Zhang et al., 2021), there are two unique energy sources to be considered in the kernel computation for either uniform or non-uniform cases: the actual (physical) source of energy as well as the detector. Following the terminology of the adjoint formalism, they are referred to as the source of forward intensity and backward intensity, respectively. We have shown that due to non-uniform scattering properties additional energy transport channels can appear between the two sources, which do not exist in the case of a uniform scattering medium. Therefore, the sensitivity kernels for non-uniform scattering media can appear rather complex. A physical interpretation of three different kernels has been proposed: (a) the decorrelation kernel is the most straightforward to interpret and has high sensitivities where the mean intensities are high; (b) the travel-time kernel shows high sensitivity where the forward and backward specific intensities are simultaneously large and in opposite direction; (c) the (intensity) scattering kernel combines the properties of both the decorrelation and travel-time kernel and has high absolute sensitivities where the energy fluxes are simultaneously large and parallel or anti-parallel. Furthermore, the pattern of positive and negative sensitivities in the scattering kernel is controlled by the scalar product of the energy current vectors from the forward and backward sources.

The interpretation of the scattering kernel, whose pattern can be strongly affected by non-uniform scattering properties, is more intuitive when considering the dominant contributions to the energy fluxes. In particular, we have carefully considered the vicinity of the sources, where the sensitivity is high. In this case, there are two types of contributions to the resulting fluxes: (a) the direct flux between the forward and backward sources and (b) the flux induced by the non-uniformity of scattering strength. The direction and magnitude of these two fluxes in turn depend on several parameters including distance from the boundary of scattering contrast, inter-source distance, orientation of the sources w.r.t. each otherb and the scattering contrast. As demonstrated in this work, knowledge of these actual fluxes is required in order to fully understand the scattering kernels.

Finally, this study visually demonstrates the strong difference between travel-time and decorrelation kernels, particularly in the case of non-uniform media with high contrast of scattering properties.

Appendix A: Calculation of Sensitivity Kernels: A Monte Carlo Simulation Approach

To compute the sensitivity kernels (see Equations A1–A3) we perform Monte Carlo simulations based on the 2D RTE with isotropic scattering. We recall that in a Monte Carlo approach (e.g., Margerin et al., 2000), the transport of energy is represented by random walks of discrete seismic "phonons" (Shearer & Earle, 2004) that undergo a sequence of collisions in a scattering and absorbing medium. In practice, the medium is often discretized onto elementary volumes where the number of phonons is monitored as a function of time to estimate the energy density. But it is also possible to compute the energy density detected at a specific point of the medium by evaluating the probability for the phonon to return to the detector at each scattering event (see, e.g., Hoshiba, 1991, for a detailed treatment). In the present work, we adopt the latter approach.

A1. Differential Monte Carlo Approach

The central idea of the differential Monte Carlo method is best explained with an example (see Lux & Koblinger, 1991, for a detailed treatment). Consider for instance the impact of a perturbation of the scattering coefficient on the energy density. Suppose that a seismic phonon has just been scattered at point $\mathbf{r}'$ in a reference medium with scattering coefficient g. The probability density function (pdf) of the position $\mathbf{r}$ of the next collision point may be written as:

$$P(\mathbf{x};\mathbf{x}'|g) = g(\mathbf{x})e^{-\int_{\mathbf{x}'}^{\mathbf{x}} g(\mathbf{x}'')d\mathbf{x}''} \tag{A1}$$

where the integral is carried on the ray connecting the point $\mathbf{x}'$ to the point $\mathbf{x}$. Note that we allow the scattering coefficient to vary spatially in the reference medium. The distribution of path length in the perturbed medium is obtained by the substitution $g \rightarrow g + \delta g$ in Equation A1. In the differential Monte Carlo method, the envelopes in the reference and perturbed medium are calculated simultaneously via a biasing scheme for the latter (Lux & Koblinger, 1991). To picture the idea, one may imagine a "true" phonon propagating in the reference medium and

a "virtual" mate following *exactly* the same trajectory as the "true" phonon albeit in the perturbed medium. As the phonon propagates in the reference medium, the statistical weight of its virtual mate is updated to compensate exactly for the genuine frequency of occurrence of the path in the perturbed medium. As an example, let us consider the change of weight occurring after the phonon has left the collision point $\mathbf{x}'$ until it is scattered again at point $\mathbf{x}$. Denoting by w the correction factor, we find:

$$w(\mathbf{x};\mathbf{x}') = \frac{P(\mathbf{x};\mathbf{x}'|g+\delta g)}{P(\mathbf{x};\mathbf{x}'|g)}$$

$$= \frac{(g(\mathbf{x})+\delta g(\mathbf{x}))e^{-\int_{\mathbf{x}'}^{\mathbf{x}}\delta g(\mathbf{x}'')dx''}}{g(\mathbf{x})}$$

An obvious condition of applicability is that $g(\mathbf{x}) > 0$, implying that a collision is indeed possible at the point $\mathbf{x}$ in the reference medium. We also remark that there is no assumption on the "smallness" of δg in the derivation of Equation A2. For the computation of sensitivity kernels, we thus further require $\delta g/g \ll 1$ and perform a Taylor expansion to obtain (Ogiso, 2019; Takeuchi, 2016):

$$w(\mathbf{x};\mathbf{x}') = 1 + \frac{\delta g(\mathbf{x})}{g(\mathbf{x})} - \int_{\mathbf{x}'}^{\mathbf{x}} \delta g(\mathbf{x}'')dx'' \tag{A2}$$

The interpretation of the above formula is as follows: as the virtual phonon propagates between the two collision points $\mathbf{x}'$ and $\mathbf{x}$, its weight decreases progressively following the integral term; at the collision point $\mathbf{x}$, its weight undergoes a positive jump $\delta g(\mathbf{x})/g(\mathbf{x})$. These two contributions may respectively be related to the loss and gain terms in Equation 3.

There are two difficulties in the practical application of Equation A2. The first one becomes apparent when one discretizes the kernel onto a grid of pixels (in 2D, or voxels in 3D): the path of the particle inside each pixel has to be carefully monitored to calculate the integral in Equation A2. Such particle tracking can be at the origin of significant computational overhead. The other difficulty is inherent to the spatial variation of the scattering coefficient. Generating the exact path length distribution for the pdf (Equation A1) involves the computation of the line integral of g which may be very time consuming. In what follows, we propose a method that solves both of these issues by transferring all the sensitivity computation to collision points. A strength of the method is that particle tracking is minimal. Furthermore, a completely arbitrary distribution of scattering properties -including discontinuities of the scattering coefficient-may be implemented transparently and in an "exact" fashion. The main drawback of the approach is that the introduction of statistical weights may result in an increase of the variance of the results. For the applications at hand, we did not find this issue to be limiting.

A2. The Method of Null or Delta Collisions

We begin by recalling a simple and very efficient method to simulate the transport of energy in an arbitrarily scattering and absorbing medium, referred to as the method of null or delta collisions (Lux & Koblinger, 1991). The starting point is the RTE:

$$(\partial_t + c\mathbf{k}\cdot\nabla + \tau(\mathbf{x})^{-1} + t_a(\mathbf{x})^{-1})e(t,\mathbf{x},\mathbf{k}) = \tau(\mathbf{x})^{-1}\int p(\mathbf{k},\mathbf{k}')e(t,\mathbf{x},\mathbf{k}')dk' \tag{A3}$$

where c, τ, t_a, and $p(\mathbf{k},\mathbf{k}')$ refer to the energy velocity, the scattering mean free time, the absorption time, and the scattering pattern, respectively. The energy density flowing in direction $\mathbf{k}$ (vector on the unit circle) at time t and position $\mathbf{x}$ is denoted by $e(t,\mathbf{x},\mathbf{k})$. The integral on the right-hand side is carried over all the directions of propagation. We remark that Equation A3 is equivalent to the following modified transport equation:

$$\begin{aligned}(\partial_t + c\mathbf{k}\cdot\nabla + \tau(\mathbf{x})^{-1} + t_a(\mathbf{x})^{-1} + \tau_\delta(\mathbf{x})^{-1})e(t,\mathbf{x},\mathbf{k}) = \\ \tau(\mathbf{x})^{-1}\int p(\mathbf{k},\mathbf{k}')e(t,\mathbf{x},\mathbf{k}')dk' + \tau_\delta(\mathbf{x})^{-1}\int \delta(\mathbf{k},\mathbf{k}')e(t,\mathbf{x},\mathbf{k}')dk'\end{aligned} \tag{A4}$$

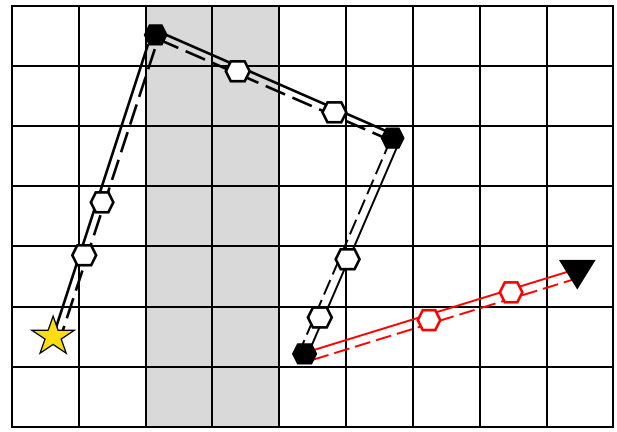

Figure A1. Graphical representation of the flexible Monte Carlo simulation employed in this study. A "true" phonon is propagating through a reference medium from the source (yellow star) to the detector (black triangle). The propagation path of the true phonon is depicted as a solid line. A "virtual" phonon is propagating in a perturbed medium and follows the exact same trajectory, depicted by the dashed line. Between source and detector, the phonons experience delta and physical scattering events (or collisions), indicated by the open and black hexagonals, respectively. This implies that we simulate more collisions than there are physical collisions. At every collision we (a) update the weights of the phonons, taking into account the non-uniformity and (b) compute the sensitivities. The red color highlights the last part of the trajectory toward the detector; in the shown example after three scattering events. The regular grid is indicated by the horizontal and vertical black lines. The simulation can take into account laterally varying scattering properties, represented by the darker pixels. For the simulations this only implies that the phonon weights at the collisions are updated differently.

which features a new scattering process with pattern $\delta(\mathbf{k}, \mathbf{k}')$ (the delta function on the unit sphere) and mean free time $\tau_\delta(\mathbf{x})$. This new process is characterized by the property that it leaves the propagation direction unchanged. It is worth emphasizing that such delta-collisions or null-collisions do not modify the statistics of true physical scattering events. Because the scattering coefficient of delta-collisions is entirely arbitrary, we may always adjust it in a way such that $\tau_\delta(\mathbf{x})^{-1} + \tau(\mathbf{x})^{-1} + t_a(\mathbf{x})^{-1} = \tau_e^{-1}$, where the extinction time τ_e is *fixed*. By adding the new scattering process, we have in effect turned a possibly complicated medium into a much simpler one where the extinction length is constant. This method has been implemented by van Dinther et al. (2021) to model the scattering of seismic waves across the North Anatolian fault zone. The price to be paid is that one has to simulate more scattering events than in the original problem. However, in the perspective of computing sensitivities, this is not necessarily a drawback. Indeed, as shown below, all the contributions to the sensitivity come exclusively from collision points in the modified numerical scheme. Figure A1 shows a graphical representation of this method.

A3. Sensitivity Computations

We begin by noting that in the numerical simulations, absorption is treated as a phonon capture event, which puts it on the same footing as a scattering event. Indeed, it is important to keep in mind that the extinction time incorporates the three possible types of interactions: physical scattering, delta scattering and absorption. Rather than terminating the phonon history after an absorption event, we assign a weight w to the particle. At each collision w is multiplied by a factor equal to the local "survival" probability of the phonon $1 - t_a(\mathbf{x})^{-1}/\tau_e^{-1}$. That this procedure correctly models the exponential decay of the intensity along its path may be demonstrated heuristically as follows. Consider two neighboring points on the ray path of a seismic phonon and denote by s a spatial coordinate on the ray. If the path length δs is sufficiently small, we may neglect multiple collision events. In this scenario, either the phonon propagates freely over δs, or it suffers from an additional collision upon which its weight is updated. Hence we have on average:

$$w(s+\delta s) = w(s)\left(1 - \frac{\delta s}{c\tau_e}\right) + w(s)\left(1 - \frac{t_a(s)^{-1}}{\tau_e^{-1}}\right)\frac{\delta s}{c\tau_e} \tag{A5}$$

where we approximate the scattering probability by $(c\tau_e)^{-1}\delta s$. Using a Taylor expansion of the left-hand side, simplifying and rearranging terms we obtain:

$$\frac{dw(s)}{ds} = -\frac{w(s)}{ct_a(s)} \tag{A6}$$

which proves the statement. The same line of reasoning will be used below to calculate the contribution of the path from the last scattering event to the detector.

Thanks to these preliminaries, it is now straightforward to apply the differential Monte Carlo method to our problem. As an illustration, let us consider the impact of a scattering perturbation $\delta\tau(\mathbf{x})^{-1}$. Again it is conceptually convenient to consider two phonons: a real phonon propagating in the reference medium and an imaginary phonon propagating in the perturbed medium. We shall also require that the perturbed and unperturbed media have the same extinction time τ_e. Since this parameter can be arbitrarily chosen, this condition can always be fulfilled. By imposing the equality of the extinction time in the reference and perturbed medium, we remove any change of the weight of the virtual phonon in between two collisions. Furthermore, our choice imposes that the rate of delta collisions in the perturbed medium be given by $\tau_\delta^{-1} - \delta\tau(\mathbf{x})^{-1}$. As a consequence, both delta collisions and physical scattering events contribute to the sensitivity to a scattering perturbation. Following the same reasoning as in the derivation of Equation A2, the weight of the virtual phonon after a delta collision at point $\mathbf{x}_c$ is updated as follows:

$$\begin{aligned} w(\mathbf{x}_c) &\rightarrow w(\mathbf{x}_c) \times \frac{\tau_\delta(\mathbf{x}_c)^{-1} - \delta\tau(\mathbf{x}_c)^{-1}}{\tau_e^{-1}} \times \frac{\tau_e^{-1}}{\tau_\delta(\mathbf{x}_c)^{-1}} \\ &\rightarrow w(\mathbf{x}_c)\left(1 - \frac{\delta\tau(\mathbf{x}_c)^{-1}}{\tau_\delta(\mathbf{x}_c)^{-1}}\right) \end{aligned} \tag{A7}$$

This last equation highlights that the rate of imaginary collisions must always be strictly positive. The same reasoning applied to a physical scattering event yields:

$$w(\mathbf{x}_c) \rightarrow w(\mathbf{x}_c)(1 + \delta\tau(\mathbf{x}_c)^{-1}/\tau(\mathbf{x}_c)^{-1}) \tag{A8}$$

Comparing Equation A2 with Equations A7 and A8, it is clear that what our method does in effect is to calculate the line integral in Equation A2 by a Monte Carlo approach, where the imaginary collisions serve as sample points for the quadrature. It is however worth noting that we did not make any smallness assumption in the derivation of Equations A7 and A8. The case of a perturbation of absorption may be treated exactly along the same lines. We find that at imaginary collisions, Equation A7 applies with the substitution $\delta\tau(\mathbf{x}_c)^{-1} \rightarrow \delta t_a(\mathbf{x}_c)^{-1}$.

The last point to be discussed concerns the treatment of the return probability of the phonon from the last scattering event at $\mathbf{x}_l$ to the detector at $\mathbf{r}$ in the method of partial summations of Hoshiba (1991). The score (or contribution) of the phonon involves the factor $e^{-\int_{\mathbf{x}_l}^{\mathbf{r}}(t_a(\mathbf{x})^{-1}+\tau(\mathbf{x})^{-1})c^{-1}dx}$ which represents the probability for the phonon to propagate from $\mathbf{x}_l$ to $\mathbf{r}$ (or beyond) without absorption or physical collisions. It is clear that any perturbation of attenuation properties affect the line integral. We could of course compute this contribution by evaluating numerically the integral but we would then lose the benefits of the transfer of the sensitivity to collision points. To remedy the difficulty, we replace the numerical quadrature by the following Monte-Carlo procedure:

1. Starting from position $\mathbf{x}_l$, randomly select the distance L to a new collision point on the ray connecting the last scattering point to the detector. Recall that the pdf of L is simply given by $(\tau_e c)^{-1}\exp(-(\tau_e c)^{-1}L)$.
2. At the collision point $\mathbf{x}_c$, modify the weight of the phonon by the factor $\tau_\delta(\mathbf{x}_c)^{-1}/\tau_e^{-1}$.
3. Compute the factors affecting the sensitivities to scattering (or absorption) following Equation A7.
4. Repeat (1) until the phonon has traveled beyond $\mathbf{r}$.

Steps 1 and 2 simulate the propagation of the phonon from $\mathbf{x}_l$ to $\mathbf{r}$ in a way such that only delta collisions can occur. The process is enforced by decreasing the weight of the particle by the factor $\tau_\delta(\mathbf{x}_c)^{-1}/\tau_e^{-1}$ at each collision. That the weight of the particle decreases on average as desired can be easily established by following the same heuristic argument as in the derivation of Equation A5. In step 3, we assume again that the total attenuation is the same in the reference and perturbed medium. Equation A7 is therefore directly applicable to the computation of the sensitivity to scattering (or absorption) perturbation on the path connecting $\mathbf{x}_l$ to $\mathbf{r}$.

In numerical applications, the kernels are discretized onto pixels whose dimensions fix the lower bound for the spatial resolution that may be achieved in an inversion. In practice, the kernel is stored as a matrix representing the grid and the scattering properties may be perturbed independently in each pixel. Every time a collision occurs, the corresponding element of the matrix is incremented with the weight perturbation of the particle, following Equation A7 and A8. This procedure allows us to monitor how each pixel influences the observable at hand. As a consequence of the discretization, the numerical kernels introduce both spatial and temporal averaging as compared to their analytical counterparts (Mayor et al., 2014). A positive consequence is that all singularities are automatically regularized, which allows for a more straightforward application of the kernels. Furthermore, whereas analytical kernels are attached to the uniform reference medium, the Monte-Carlo approach lends itself naturally to an iterative linearized inversion procedure. From a numerical perspective, the most important feature of our method is the high degree of flexibility, which allows one to very simply model arbitrary non-uniform scattering and absorbing medium, including the presence of discontinuities in the model parameters. We believe that this simplicity largely balances the slowdown entailed by the simulation of artificial scattering events.

For the simulations shown in this manuscript we use a grid of 76×76 pixels, where each of the pixels has a dimension of 4 km $\times$ 4 km. The kernel is evaluated every second, up to a maximum lapse-time of 120 s. The final temporal resolution, however, is 5 s, due to the application of a 5 s moving window to average the kernels and reduce the statistical fluctuations. The total number of phonons simulated for each model is 4×10^9. The distance between the sources, R, equals 32 km for most models (uniform and half-space case), with the placement of the sources at the center of the pixels. For all simulations the full grid space has a uniform value for the intrinsic quality factor $Q_i^{uni} = 100$, based on values recently derived for a normal crustal setting in Turkey, in the vicinity of the Izmit rupture zone (e.g., van Dinther et al., 2021). The scattering mean free path varies depending on the model.

Data Availability Statement

The code used for the numerical simulations is publicly available at https://zenodo.org/; Margerin & van Dinther, 2021.

Acknowledgments
We acknowledge the support from the European Research Council (ERC) under the European Union's Horizon 2020 research and innovation program (Grant Agreement No. 742 335, F-IMAGE). This work was granted access to the HPC resources of CALMIP supercomputing center (https://www.calmip.univ-toulouse.fr) under the allocation 2020-p19038, where the majority of the simulations have been run. Some of the computations presented in this paper were performed using the CIMENT infrastructure (https://gricad.univ-grenoble-alpes.fr), which is supported by the Rhône-Alpes region (Grant CPER07_13 CIRA and France-Grille (http://www.france-grilles.fr)).

References

Arridge, S. R. (1995). Photon-measurement density functions. Part I: Analytical forms. *Applied Optics*, *34*(31), 7395–7409. https://doi.org/10.1364/ao.34.007395

Barajas, A. (2021). *Imaging for scattering properties of the crust: Body to surface waves coupling* (Unpublished doctoral dissertation).

Brenguier, F., Campillo, M., Hadziioannou, C., Shapiro, N. M., Nadeau, R. M., & Larose, E. (2008). Postseismic relaxation along the San Andreas Fault at Parkfield from continuous seismological observations. *Science*, *321*(5895), 1478–1481. https://doi.org/10.1126/science.1160943

Brenguier, F., Rivet, D., Obermann, A., Nakata, N., Boué, P., Lecocq, T., et al. (2016). 4-D noise-based seismology at volcanoes: Ongoing efforts and perspectives. *Journal of Volcanology and Geothermal Research*, *321*, 182–195. https://doi.org/10.1016/j.jvolgeores.2016.04.036

Chen, J. H., Froment, B., Liu, Q. Y., & Campillo, M. (2010). Distribution of seismic wave speed changes associated with the 12 may 2008 mw 7.9 Wenchuan earthquake. *Geophysical Research Letters*, *37*(18). https://doi.org/10.1029/2010gl044582

Duran, A., Planes, T., & Obermann, A. (2020). Coda-wave decorrelation sensitivity kernels in 2-d elastic media: A numerical approach. *Geophysical Journal International*, *223*(2), 934–943. https://doi.org/10.1093/gji/ggaa357

Gaebler, P., Eken, T., Bektaş, H. Ö., Eulenfeld, T., Wegler, U., & Taymaz, T. (2019). Imaging of shear wave attenuation along the central part of the North Anatolian Fault Zone, Turkey. *Journal of Seismology*, *23*(4), 913–927. https://doi.org/10.1007/s10950-019-09842-1

Hillers, G., Husen, S., Obermann, A., Planes, T., Larose, E., & Campillo, M. (2015). Noise-based monitoring and imaging of aseismic transient deformation induced by the 2006 Basel reservoir stimulation. *Geophysics*, *80*(4), KS51–KS68. https://doi.org/10.1190/geo2014-0455.1

Hillers, G., Vuorinen, T., Uski, M. R., Kortström, J. T., Mäntyniemi, P. B., Tiira, T. et al. (2020). The 2018 geothermal reservoir stimulation in Espoo/Helsinki, southern Finland: Seismic network anatomy and data features. *Seismological Research Letters*, *91*(2A), 770–786. https://doi.org/10.1785/0220190253

Hirose, T., Nakahara, H., & Nishimura, T. (2017). Combined use of repeated active shots and ambient noise to detect temporal changes in seismic velocity: Application to Sakurajima volcano, Japan. *Earth Planets and Space*, *69*(1), 42. https://doi.org/10.1186/s40623-017-0613-7

Hirose, T., Nakahara, H., & Nishimura, T. (2019). A passive estimation method of scattering and intrinsic absorption parameters from envelopes of seismic ambient noise cross-correlation functions. *Geophysical Research Letters*, *46*(7), 3634–3642. https://doi.org/10.1029/2018gl080553

Hoshiba, M. (1991). Simulation of multiple-scattered coda wave excitation based on the energy conservation law. *Physics of the Earth and Planetary Interiors*, *67*(1–2), 123–136. https://doi.org/10.1016/0031-9201(91)90066-q

Kanu, C., & Snieder, R. (2015a). Numerical computation of the sensitivity kernel for monitoring weak changes with multiply scattered acoustic waves. *Geophysical Journal International*, *203*(3), 1923–1936. https://doi.org/10.1093/gji/ggv391

Kanu, C., & Snieder, R. (2015b). Time-lapse imaging of a localized weak change with multiply scattered waves using numerical-based sensitivity kernel. *Journal of Geophysical Research: Solid Earth*, *120*(8), 5595–5605. https://doi.org/10.1002/2015jb011871

Lux, I., & Koblinger, L. (1991). *Monte Carlo particle transport methods: Neutron and photon calculations*. CRC Press.

Mao, S., Campillo, M., van der Hilst, R. D., Brenguier, F., Stehly, L., & Hillers, G. (2019). High temporal resolution monitoring of small variations in crustal strain by dense seismic arrays. *Geophysical Research Letters*, *46*(1), 128–137. https://doi.org/10.1029/2018gl079944

Margerin, L. (2005). Introduction to radiative transfer of seismic waves. *Geophysical Monograph-American Geophysical Union*, *157*, 229. https://doi.org/10.1029/157gm14

Margerin, L., Bajaras, A., & Campillo, M. (2019). A scalar radiative transfer model including the coupling between surface and body waves. *Geophysical Journal International*, *219*(2), 1092–1108. https://doi.org/10.1093/gji/ggz348

Margerin, L., Campillo, M., & Van Tiggelen, B. (2000). Monte Carlo simulation of multiple scattering of elastic waves. *Journal of Geophysical Research: Solid Earth*, *105*(B4), 7873–7892. https://doi.org/10.1029/1999jb900359

Margerin, L., Planes, T., Mayor, J., & Calvet, M. (2016). Sensitivity kernels for coda-wave interferometry and scattering tomography: Theory and numerical evaluation in two-dimensional anisotropically scattering media. *Geophysical Journal International*, *204*(1), 650–666. https://doi.org/10.1093/gji/ggv470

Margerin, L., & van Dinther, C. (2021). *Coda wave sensitivity kernels for non-uniform scattering media: The Monte Carlo simulation code*. Zenodo. https://doi.org/10.5281/zenodo.495751710.5281/zenodo.4957517

Mayor, J., Margerin, L., & Calvet, M. (2014). Sensitivity of coda waves to spatial variations of absorption and scattering: Radiative transfer theory and 2-D examples. *Geophysical Journal International*, *197*(2), 1117–1137. https://doi.org/10.1093/gji/ggu046

Mordret, A., Jolly, A., Duputel, Z., & Fournier, N. (2010). Monitoring of phreatic eruptions using interferometry on retrieved cross-correlation function from ambient seismic noise: Results from Mt. Ruapehu, New Zealand. *Journal of Volcanology and Geothermal Research*, *191*(1–2), 46–59. https://doi.org/10.1016/j.jvolgeores.2010.01.010

Obermann, A., Kraft, T., Larose, E., & Wiemer, S. (2015). Potential of ambient seismic noise techniques to monitor the St. Gallen geothermal site (Switzerland). *Journal of Geophysical Research: Solid Earth*, *120*(6), 4301–4316. https://doi.org/10.1002/2014jb011817

Obermann, A., Planès, T., Hadziioannou, C., & Campillo, M. (2016). Lapse-time-dependent coda-wave depth sensitivity to local velocity perturbations in 3-D heterogeneous elastic media. *Geophysical Journal International*, *207*(1), 59–66. https://doi.org/10.1093/gji/ggw264

Obermann, A., Planès, T., Larose, E., & Campillo, M. (2013). Imaging preeruptive and coeruptive structural and mechanical changes of a volcano with ambient seismic noise. *Journal of Geophysical Research: Solid Earth*, *118*(12), 6285–6294. https://doi.org/10.1002/2013jb010399

Obermann, A., Planès, T. Larose, E., & Campillo, M. (2019). 4-D imaging of subsurface changes with coda waves: Numerical studies of 3-D combined sensitivity kernels and applications to the m_w 7.9, 2008 Wenchuan earthquake. *Pure and Applied Geophysics*, *176*(3), 1243–1254. https://doi.org/10.1007/s00024-018-2014-7

Obermann, A., Planès, T., Larose, E., Sens-Schönfelder, C., & Campillo, M. (2013b). Depth sensitivity of seismic coda waves to velocity perturbations in an elastic heterogeneous medium. *Geophysical Journal International*, *194*(1), 372–382. https://doi.org/10.1093/gji/ggt043

Ogiso, M. (2019). A method for mapping intrinsic attenuation factors and scattering coefficients of s waves in 3-d space and its application in southwestern japan. *Geophysical Journal International*, *216*(2), 948–957. https://doi.org/10.1093/gji/ggy468

Paasschens, J. (1997). Solution of the time-dependent Boltzmann equation. *Physical Review E*, *56*(1), 1135. https://doi.org/10.1103/physreve.56.1135

Pacheco, C., & Snieder, R. (2005). Time-lapse travel time change of multiply scattered acoustic waves. *Journal of the Acoustical Society of America*, *118*(3), 1300–1310. https://doi.org/10.1121/1.2000827

Pacheco, C., & Snieder, R. (2006). Time-lapse traveltime change of singly scattered acoustic waves. *Geophysical Journal International*, *165*(2), 485–500. https://doi.org/10.1111/j.1365-246x.2006.02856.x

Peng, Z., & Ben-Zion, Y. (2006). Temporal changes of shallow seismic velocity around the Karadere-düzce branch of the north Anatolian fault and strong ground motion. *Pure and Applied Geophysics*, *163*(2–3), 567–600. https://doi.org/10.1007/s00024-005-0034-6

Planès, T., Larose, E., Margerin, L., Rossetto, V., & Sens-Schönfelder, C. (2014). Decorrelation and phase-shift of coda waves induced by local changes: Multiple scattering approach and numerical validation. *Waves in Random and Complex Media*, *24*(2), 99–125. https://doi.org/10.1080/17455030.2014.880821

Poupinet, G., Ellsworth, W., & Frechet, J. (1984). Monitoring velocity variations in the crust using earthquake doublets: An application to the Calaveras Fault, California. *Journal of Geophysical Research: Solid Earth*, *89*(B7), 5719–5731. https://doi.org/10.1029/jb089ib07p05719

Rivet, D., Campillo, M., Radiguet, M., Zigone, D., Cruz-Atienza, V., Shapiro, N. M., et al. (2014). Seismic velocity changes, strain rate and non-volcanic tremors during the 2009–2010 slow slip event in Guerrero, Mexico. *Geophysical Journal International*, *196*(1), 447–460. https://doi.org/10.1093/gji/ggt374

Roux, P., & Ben-Zion, Y. (2014). Monitoring fault zone environments with correlations of earthquake waveforms. *Geophysical Journal International*, *196*(2), 1073–1081. https://doi.org/10.1093/gji/ggt441

Sánchez-Pastor, P., Obermann, A., & Schimmel, M. (2018). Detecting and locating precursory signals during the 2011 El Hierro, Canary Islands, submarine eruption. *Geophysical Research Letters*, *45*(19), 10–288.

Sato, H. (1993). Energy transportation in one-and two-dimensional scattering media: Analytic solutions of the multiple isotropic scattering model. *Geophysical Journal International*, *112*(1), 141–146. https://doi.org/10.1111/j.1365-246x.1993.tb01443.x

Schaff, D. P., & Beroza, G. C. (2004). Coseismic and postseismic velocity changes measured by repeating earthquakes. *Journal of Geophysical Research: Solid Earth*, *109*B10

Sens-Schönfelder, C., Bataille, K., & Bianchi, M. (2021). High frequency (6 Hz) PKPab precursors and their sensitivity to deep earth heterogeneity. *Geophysical Research Letters*, *48*, e2020GL089203.

Sens-Schönfelder, C., & Wegler, U. (2006). Passive image interferometry and seasonal variations of seismic velocities at Merapi Volcano, Indonesia. *Geophysical Research Letters*, *33*(21). https://doi.org/10.1029/2006gl027797

Shearer, P. M., & Earle, P. S. (2004). The global short-period wavefield modelled with a Monte Carlo seismic phonon method. *Geophysical Journal International*, *158*(3), 1103–1117. https://doi.org/10.1111/j.1365-246x.2004.02378.x

Snieder, R., Duran, A., & Obermann, A. (2019). Locating velocity changes in elastic media with coda wave interferometry. In: N. Nakata, L. Gualtieri, & A. Fitchtner, (Eds.), *Seismic ambient noise* (pp. 188–217). Cambridge University Press.

Snieder, R., Grêt, A., Douma, H., & Scales, J. (2002). Coda wave interferometry for estimating nonlinear behavior in seismic velocity. *Science*, *295*(5563), 2253–2255. https://doi.org/10.1126/science.1070015

Takeuchi, N. (2016). Differential Monte Carlo method for computing seismogram envelopes and their partial derivatives. *Journal of Geophysical Research: Solid Earth*, *121*(5), 3428–3444. https://doi.org/10.1002/2015jb012661

van Dinther, C., Margerin, L., & Campillo, M. (2021). Laterally varying scattering properties in the North Anatolian Fault Zone from ambient noise cross-correlations. *Geophysical Journal International*, *225*(1), 589–607. https://doi.org/10.1093/gji/ggaa606

Wegler, U., & Lühr, B. G. (2001). Scattering behaviour at merapi volcano (java) revealed from an active seismic experiment. *Geophysical Journal International*, *145*(3), 579–592. https://doi.org/10.1046/j.1365-246x.2001.01390.x

Wilson, B. C., & Adam, G. (1983). A Monte Carlo model for the absorption and flux distributions of light in tissue. *Medical Physics*, *10*(6), 824–830. https://doi.org/10.1118/1.595361

Wu, C., Peng, Z., & Ben-Zion, Y. (2009). Non-linearity and temporal changes of fault zone site response associated with strong ground motion. *Geophysical Journal International*, *176*(1), 265–278. https://doi.org/10.1111/j.1365-246x.2008.04005.x

Yamamoto, M., & Sato, H. (2010). Multiple scattering and mode conversion revealed by an active seismic experiment at asama volcano, japan. *Journal of Geophysical Research: Solid Earth*, *115*(B7). https://doi.org/10.1029/2009jb007109

Yoshimoto, K., Wegler, U., & Korn, M. (2006). A volcanic front as a boundary of seismic-attenuation structures in northeastern Honshu, Japan. *Bulletin of the Seismological Society of America*, *96*(2), 637–646. https://doi.org/10.1785/0120050085

Zhang, T., Sens-Schönfelder, C., & Margerin, L. (2021). Sensitivity kernels for static and dynamic tomography of scattering and absorbing media with elastic waves: A probabilistic approach. *Geophysical Journal International*. https://doi.org/10.1093/gji/ggab048